Towards an understanding of the electron paramagnetic resonance spectra of the ferritin core

A study of human liver ferritin

by

Vera Čaluković

to obtain the degree of Master of Science
in Biomedical Engineering
at the Delft University of Technology,
to be defended publicly on Tuesday November 3, 2020 at 13:30.

Student number:	4713419	
Project duration:	December 10, 2019 – November 2, 2020	
Thesis committee:	Prof. F. M. Vos,	TU Delft, committee chair
	Prof. H. S. J. van der Zant	TU Delft, committee member and supervisor
	MSc. J. A. Labra-Muñoz	TU Delft/LION, committee member and daily supervisor
	Dr. L. Bossoni	LUMC, daily supervisor
	Dr. M. I. Huber	LION, supervisor

This thesis is confidential and cannot be made public until 3 November, 2021.

Abstract

Ferritin is the main iron storage protein in mammals. Its mineral composition, magnetic properties and electronic structure have yet to be unravelled. However, it is generally agreed that the mineral core is composed of ferrihydrite, and that the particle features a transition to antiferromagnetic order above room temperature, and has superparamagnetic properties from room temperature to the blocking temperature.

A technique that can be used in the study of the magnetic properties of ferritin is electron paramagnetic resonance (EPR), which is sensitive to the magnetic moments of unpaired electrons.

The magnetic properties of human liver ferritin were studied using 9 GHz EPR, with which temperature dependent spectra were acquired in the following range: 5-150 K. A novel approach, typically used in magnetic resonance spectroscopy, was employed to pre-process the baseline-corrected spectra and remove features for which it was unlikely to originate from the ferritin core. This allowed for the isolation and preservation of the general lineshape of the signal belonging to the ferritin core.

The spectra were further analysed using both a phenomenological approach and by employing the Spin Hamiltonian.

The phenomenological analysis showed that in the 20-70 K temperature range, the amplitude peak-to-peak of the ferritin-core signal decreases linearly with decreasing temperature, while its lineshape changes from Lorentzian to Gaussian between 150 and 70 K. The blocking temperature was suggested to occur between 10 and 20 K, where the signal amplitude was lost.

Whether and how the lineshape of the ferritin core signal shifts or broadens below 70 K could not be determined due to a six-line signal contamination, most likely caused by manganese impurities, obscuring the ferritin-core signal in the field range where its resonance field is positioned.

In order to study the magnetic properties of the ferritin core, and therefore gain insight on the magnetic and electronic structure of the ferritin core, a Spin Hamiltonian approach was employed. The simplified Giant Spin Hamiltonian model featured a single spin system with total spin $S = 10$. This analysis suggests that the ferritin-core signal is centred at g'=2.0154, hinting at a core composition of magnetite or maghemite, rather than of ferrihydrite.

An almost fully automated procedure to pre-process a set of human liver ferritin EPR spectra obtained at different temperatures is described in this thesis.

Acknowledgements

Especially during this trying time of the COVID-pandemic, it was difficult to remain as focused on a project as one would be when working from their official office. That holds for everyone, including me. It struck especially hard considering I had just finished my literature review and was supposed to start with the practical aspect of the project and perform measurements at the lab. Luckily, it was possible to change the project within the same topic of study. During the early summer months I even got the opportunity to perform, during six days, my own measurements. This would not have been possible without the support from Jacqueline Labra-Muñoz - who made sure the setup was operable during these days, and helped me perform the measurements - and my dear friend Lisette Cuiper – who invited me into her home in Leiden so I could spend the measurement days optimally.

This thesis would not have been possible without the help of my supervisors in Leiden: Lucia Bossoni, Jacqueline Labra-Muñoz and Martina Huber. They accepted me into their groups and proposed this project when it became clear that the previously planned projects would, due to the circumstances, no longer be feasible. I would like to give special thanks to Jacqueline, who taught me much about the lab, and with whom I've had many insightful conversations – including about topics outside the scope of the project. Your enthusiasm is contagious. The same goes for Lucia, who always provided insightful feedback and made me feel like both a student and a colleague. It was very pleasant working with you.

I would also like to thank my supervisor Herre van der Zant, from Delft, for his advice and always asking the right questions during our meetings.

Also would I like to thank my colleagues, both at the Gorter Centre at the LUMC and at the physics lab at LION, for making me feel welcome whenever I was there. Special thanks go to Itamar Ronen from the LUMC, who provided me with his code so I could use it as part of the pre-processing.

Of course without my friends and family this project would never have been a success either, as one needs to have a good work-rest balance in life in order to make evident progress. I would like to thank my friends, with whom I've had many a weekly Skype meeting – all of which were extremely welcome, both for dealing with hardships and sharing joy. The projects are piling up, and this tradition should continue even after the pandemic is resolved.

Immense thanks go to my loving boyfriend Kevin Pancras - who always supports me and with whom I've had many meaningful discussions about the project conducted -, to our two cats - who always provided us with welcome distractions and warm attentions –, and to my parents and grandparents - who have always supported me in life, and by giving valuable advice helped me become the person I am today.

List of Figures

Nomenclature and Abbreviations

Abbreviations

AFM antiferromagnetism/antiferromagnetic

CW-EPR continuous-wave EPR

EELS electron energy loss spectroscopy

EPR electron paramagnetic resonance

FID free induction decay

GSH Giant Spin Hamiltonian

HoSF horse spleen ferritin

HRTEM high-resolution transmission electron microscopy

HSVD Hankel singulat value decomposition

HuLiFt human liver ferritin

ICP-MS inductively coupled plasma mass spectroscopy

lwpp linewidth peak-to-peak - phenomenological parameter in Spin Hamiltonian fitting

MNM molecular nanomagnets

MNP magnetic nanoparticles

SNR signal-to-noise ratio

SPM superparamagnetism/superparamagnetic

SQUID magnetometry superconducting quantum interference device magentometry

ZFS zero-field-splitting

Nomenclature

ΔB_{pp} resonance broadening

$\hat{H}$ Hamiltonian component

μ magnetic moment

μ_B Bohr magneton

A_{pp} amplitude peak-to-peak

B applied magnetic field

B_0 resonance field free electron

B_A anisotropy field

B_{res} resonance field

D axial ZFS term

D_x, D_y, D_z principal components of ZFS-tensor **D**

E rhombic ZFS term

g' effective g-tensor

g_e g-tensor of the free electron

k_B Boltzmann constant

S spin tensor

S_x, S_y, S_z principal components of spin tensor S

T_B blocking temperature

D ZFS-tensor

g Landé g-tensor

Contents

1

Introduction

Ferritin is the main iron storage protein within the mammalian body, and has been a subject of study over the past 70 years - both in (bio)medical fields (e.g. [1, 8, 28, 36]) and in the field of condensed-matter physics (e.g. [12, 16, 33]). Ferritin consists of a protein shell and an inorganic core. The former takes up free Fe^{2+} [25], converts it to Fe^{3+}, mineralizes it and stores it within the core in a safe form. In case of an empty core, the protein is referred to as apoferritin. Although it is thought that the core is made up of pure ferrihydrite, an iron-hydroxide which contains iron in the form of Fe^{3+} only, studies suggest that also iron-oxides such as magnetite and/or maghemite might make up a small portion of the core (e.g. [2, 29]).

Typically, 4500 iron atoms per ferritin is considered to be the maximum capacity *in vitro*, and average loading *in vivo* is generally reported to be between 1000 and 1500 iron atoms (see refs 70, 71 in [6]). The iron atoms forming the mineral core are magnetically coupled, and each iron atom has a maximum spin S of 5/2. In the case of ferromagnetic coupling, the cumulative spin S of the core can therefore exceed the order of 10^3.

Due to the nanometer size of the core, the magnetic coupling is fully detectable only below a critical temperature. This temperature is called the blocking temperature T_B, and is lower than the Néel or Curie temperature of the bulk mineral. Above the blocking temperature a paramagnetic behaviour is observed, referred to as superparamagnetism (SPM). For more information on the blocking temperature, the reader is referred to Sections 3.1 and 3.3 in Appendix C and the references therein.

Brooks et al. proposed, in 1998, a model to describe the magnetic properties of the ferritin core. According to this model, the ferritin core is composed of two layers [5]: an inner and an outer layer. The inner layer is antiferromagnetic (AFM) already above room temperature. However, defect sites within the crystal lattice are responsible for uncoupled spins which confer a SPM behaviour to the core. The outer layer is weakly AFM and retains a paramagnetic behaviour in a large temperature range. Due to the core size, however, it has been suggested that the AFM coupled core might be considered weakly ferromagnetic [35].

The main iron sources found inside the ferritin core are described in table 1.1. Also mentioned are the magnetic orders they display. For more information on the respective minerals the reader is referred to Appendix C and the references therein.

Measurement of changes in magnetic properties of the ferritin core could potentially provide insight into the onset of neurodegenerative diseases, since it has been suggested that a dysfunction of ferritin proteins plays a role in the development thereof [28]. In the brain, for example, iron accumulates with age [8]. However, in case of pathology [8] regional iron levels are elevated compared to these regions in age-matched healthy subjects.

Table 1.1: Possible iron forms of the ferritin core (diameter 5-8 nm), their magnetic order below blocking temperature (when present) and the type of iron ions the minerals consist of.

	Name	**Magnetic order**	**Iron contained**
Minerals			
$Fe_2O_3 \cdot 0.5H_2O$	ferrihydrite	antiferromagnetic (?)	Fe(III)
Fe_3O_4	magnetite	ferrimagnetic	Fe(II) and Fe(III)
γ-Fe_2O_3	maghemite	ferrimagnetic	Fe(II) and Fe(III)

The apoferritin composition is thought to dictate the main function (iron conversion, storage and mineralization) of the ferritin protein (see Section 1 in Appendix C and the references therein). Also the composition of apoferritin in the targeted brain regions seem to be differently affected by disease progression than by ageing [8], which as a result affects the core composition. In, for example, ferritin cores in the brains of Alzheimer's Disease patients, larger concentrations of magnetite and hematite are found than in ferritin in healthy brains, which are abundant in ferrihydrite [6, 28].

As of yet, the composition, magnetic properties, and electronic structure of the ferritin core have not yet been unravelled. A technique that can be used in the study of the magnetic properties of ferritin is electron paramagnetic resonance (EPR), which is sensitive to the magnetic moments of unpaired electrons. The general workings of EPR are explained in Section 3.2.1 of Appendix C.

In this thesis the magnetic properties of human liver ferritin (HuLiFt) were studied using 9 GHz continuous-wave (CW)-EPR, with which temperature dependent spectra were acquired. The spectra were processed before analysis using an ad-hoc baseline-correction technique. A novel approach, typically used in magnetic resonance spectroscopy, was employed to further process the baseline-corrected spectra. The pre-processing procedure used was developed using both horse spleen ferritin (HoSF) spectra from [20] - which are shown in Appendix B - and the HuLiFt spectra acquired for this thesis. The HuLiFt spectra were described using a phenomenological approach. Additionally, EPR spectrum simulations using the Giant Spin Hamiltonian (GSH) were described. It was hypothesized that the signal of the ferritin core of HuLiFt would, similarly to the signal in HoSF, belong to ferrihydrite. This is because both ferritins originate from organs in which the main function of the ferritin is the same, and the core of HoSF is shown to be composed of ferrihydrite [2, 23, 35].

In Section 2 theoretical background on the Spin Hamiltonian and the GSH are provided. The samples and procedures used in this study are described in Section 3. Subsequently, the EPR spectra and their analyses are presented in Section 4, and discussed in Section 5. Finally, conclusions and recommendations are given in Section 6.

2

Theory

2.1. The Spin Hamiltonian

The Spin Hamiltonian approach is widely used in the interpretation and classification of EPR spectra [14], and is built up by several interaction terms, as indicated in equation 2.1 [32].

$$\hat{H} = \sum_i [\hat{H}_{e^- - Zeeman}(i) + \hat{H}_{ZFS}(i)] + \sum_k [\hat{H}_{n-Zeeman}(k) + \hat{H}_{n-Quadrupole}(k)] + \sum_i \sum_{j>i} \hat{H}_{e^- - e^-}(i,j) + \sum_i \sum_k \hat{H}_{Hyperfine}(i,k) \tag{2.1}$$

In equation 2.1 i and j are indicative of electron spins, while k refers to nuclear spins. The first term is the electron Zeeman interaction, which is defined as

$$\hat{H}_{e^- - Zeeman}(i) = \mathbf{g}\mu_B(\mathbf{B} \cdot \mathbf{S}_i), \tag{2.2}$$

and describes the interactions between unpaired electrons and an externally applied magnetic field **B**. Here, μ_B is the Bohr magneton, **g** the Landé tensor - generally referred to as effective g (g'), or g-factor when the tensor is isotropic - and S the electron spin operator.

The zero-field-splitting (ZFS) is the second term introduced in equation 2.1, and is defined as

$$\begin{aligned} \hat{H}_{ZFS} &= \mathbf{S} \cdot \mathbf{D} \cdot \mathbf{S} \\ &= D(S_z^2 - S(S+1)/3) + E(S_x^2 - S_y^2), \end{aligned} \tag{2.3}$$

where **D** is a symmetric, traceless tensor containing the interaction terms of the system.

The third term in equation 2.1 is the nuclear Zeeman interaction, and describes the interaction of the nuclear spin I with the external magnetic field. The fourth and fifth term refer to the nuclear quadrupolar interaction and the electron-electron interaction respectively. The nuclear quadrupolar interaction describes the interactions that occur when the electric quadrupole moment of nuclei with spin $I > 1/2$ interact with the local electric field gradient at the nucleus [32]. The sixth term refers to the hyperfine interactions that result from the interactions of nuclear spins I with the magnetic moment of the unpaired electrons, related by a hyperfine coupling tensor A in MHz.

The first two terms are discussed in more detail below, as those are the main terms considered throughout the analysis of EPR spectra described in this thesis. Higher-order terms are included in the description of the particle anisotropy analysis, if the anisotropy introduced by the ZFS is insufficient [11].

2.1.1. Electron Zeeman interactions

The electron Zeeman interaction describes how much the spin energy levels associated with a spin multiplet (m_s) are split with increasing external magnetic field. This causes energy transitions between spin states to occur at specific field strengths. In figure 2.1a the energy levels are indicated for an S=1/2 spin system and isotropic g=2.25, where B is parallel to the symmetry axis of a molecule. As can be seen, the energy difference between the m_s-states - $m_s = -1/2$ and $m_s = +1/2$ - increases with increasing B strength.

The g-tensor of the system is indicative of the environment of the unpaired electron and originates from the total spin angular momentum and orbital momentum. When the energy difference between two m_s-states equals the energy delivered by the microwave frequency, an energy level transition takes place at the corresponding magnetic field strength. Such transitions are called either "allowed" (when $\Delta m_s = \pm 1$) or "forbidden" (when $|\Delta m_s| > 1$). The powder spectrum - the spherically weighted sum of spectra of an ensemble of randomly ordered paramagnetic centres - corresponding with the energy levels in figure 2.1a is shown in figure 2.1b. The signal is characterized by a single band, corresponding to the allowed transition indicated in 2.1a. In case the diagonalized g-tensor is axial - i.e. when $g_{xx} = g_{yy} \neq g_{zz}$ - two bands appear in the spectrum, as is shown in figure 2.1c. The combined signal of $g_{xx} = g_{yy}$ is indicated as $g_\perp$, being perpendicular to the applied magnetic field, while the component parallel to the applied magnetic field, g_{zz}, is indicated as $g_{//}$. As can be seen in figure 2.1c, the signal amplitude of the parallel component is lower than that of the perpendicular component. The signal is composed of three bands when each principal component of the g-tensor is unique, as is shown in figure 2.1d. This system is called rhombic.

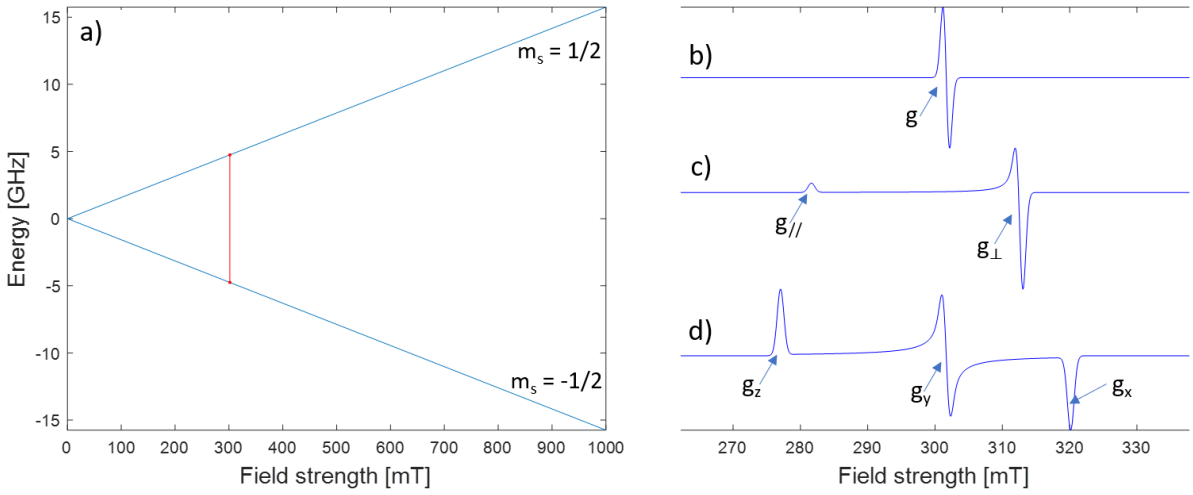

Figure 2.1: Energy levels of an S=1/2 system with isotropic ($g_{xx} = g_{yy} = g_{zz} = 2.25$) g-tensor, projected as $B//g_{zz}$ (a). First derivative EPR powder spectra of an S=1/2 system characterised by an isotropic ($g_{xx} = g_{yy} = g_{zz} = 2.25$) (b), axial ($g_{xx} = g_{yy} = 2.17, g_{zz} = 2.41$) (c) and rhombic ($g_{xx} = 2.12, g_{yy} = 2.25, g_{zz} = 2.45$) (d) g-tensor. Indicated by the arrows is the location of each corresponding g-component. Powder spectra have 1 mT Gaussian lineshape broadening.

2.1.2. Zero field splitting

The energy difference between m_s-states can also be increased in the absence of an external magnetic field. This occurs in systems of spin ground state S > 1/2, i.e. in systems with multiple unpaired electrons. In these systems, magnetic dipole-dipole interactions can cause energy state splitting in the absence of an externally applied field. This interaction is therefore named zero-field-splitting.

The origin of ZFS can be twofold - it is caused either by dipolar coupling or by spin-orbit coupling [14]. In the latter case, which holds for d- and f-orbitals of metal ions, **D** is defined as

$$\mathbf{D} = \zeta(\mathbf{g} - g_e\mathbf{I})/2, \tag{2.4}$$

by derivation from equations 2.38 and 2.40 in [14]. In equation 2.4, ζ is proportional to the spin-orbit coupling constant λ, g_e is the g-factor of the free electron, equal to 2.00231, and **I** is the identity matrix. ζ is positive for the d^n configuration for n<5, and negative for this configuration for n>5 [14]. For n=5 ζ equals zero. The effect of this sign is felt in simulations mainly at very low temperatures.

The principal components of the **D**-tensor - D_x, D_y, D_z - are defined in the eigenframe of the paramagnetic centre. Since **D** is traceless, the principal components can be cast into two parameters, D and E - see equation 2.3 -, such that

$$D = 3D_z/2, \tag{2.5}$$

and

$$E = (D_x - D_y)/2. \tag{2.6}$$

The rhombicity (E/D) should not exceed 1/3. The axes definition is chosen such that when two of the principal components of **D** are identical, the system under study is axially symmetric, and therefore E vanishes. If **D** has three unique principal components, i.e. a system in which $E \neq 0$, the **D**-tensor is rhombic.

The effect of D and E, each in mT, on the energy levels and powder spectra of an S=1 isotropic g=2 system is shown in figure 2.2. Comparison of figures 2.2a and 2.2b shows the effect of introducing axial symmetry - changes in D_z result in either an increase or a decrease of the separation between the energy levels in the energy level plots at zero magnetic field. A change in D_x and/or D_y results in the inclusion of E, an effect observed as a complete lifting of the degeneracy of all three energy levels at zero field, as can be seen in figure 2.2c. Subsequently, these changes result in a change of field strengths at which energy transitions occur when an external magnetic field is applied. This can also be observed by comparing the lineshapes of the corresponding powder spectra, shown in figures 2.2d-f. The spectra in black show the transitions at the resonance fields. Observing the more Gaussian lineshape broadened spectra, in red, it can be seen that with increasing **D**-tensor anisotropy the spectra become broader, and as a result the signal amplitude decreases.

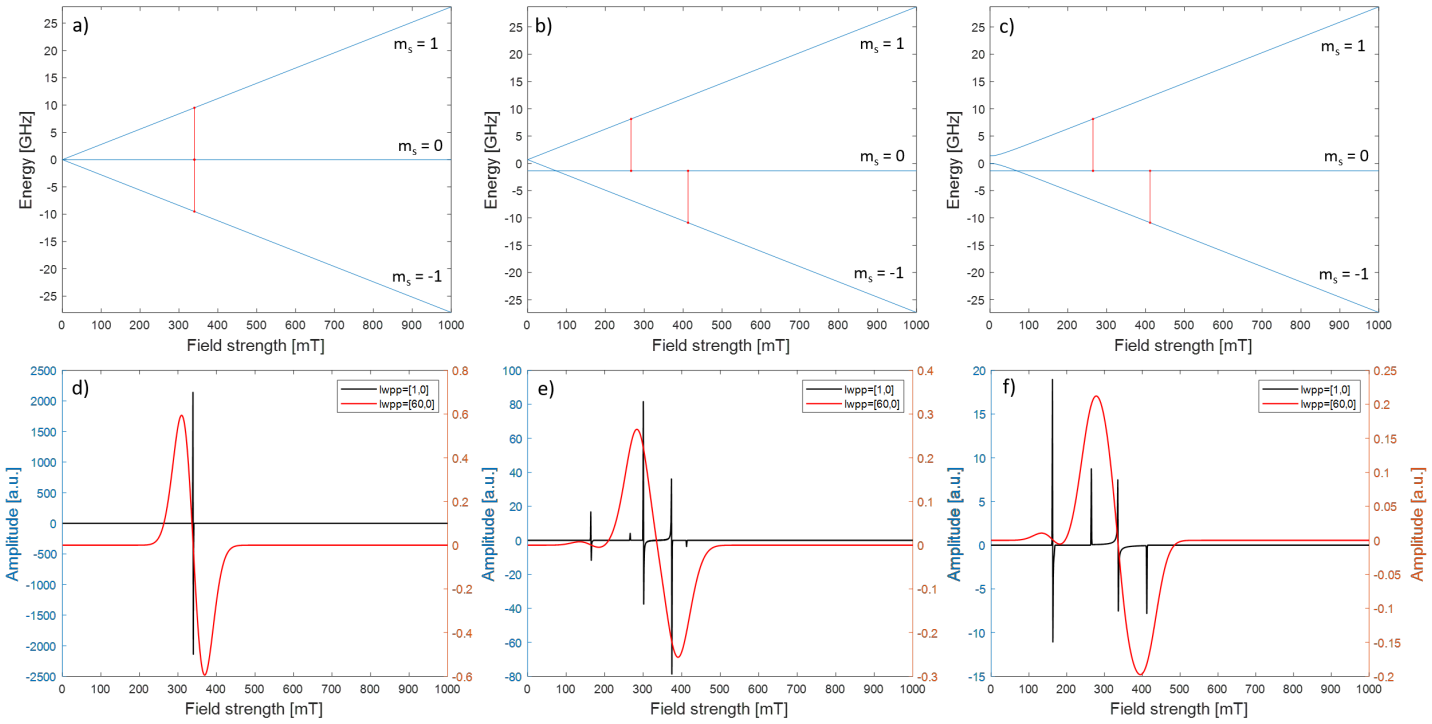

Figure 2.2: Energy levels (a-c), projected as $B//g_{zz}$, and powder spectra (d-f) of an S=1 system with isotropic g=2. The separation between energy levels can be seen with respect to an increasing external magnetic field (the Zeeman effect) and under influence of ZFS **D**, at B=0. In a) and d), only the Zeeman effect is observed. In b,e and c,f additionally the effect of D and E is perceived. b,e): D=2050 MHz, E=0 MHz; c,f): D=2050 MHz, E=2050/3 MHz. For all simulations, lwpp was set to [1,0] (black) or [60,0] (red).

2.2. On magnetic properties of nanoparticles

Nanoparticles can be composed of multiple magnetic centres, and therefore multiple coupled spin systems. Depending on the amount of magnetic centres, the nanoparticles are referred to as either molecular nanomagnets (MNM) or as magnetic nanoparticles (MNP) [11]. MNM are molecules with one to 100 magnetic centres, and are analysed using a quantum mechanical approach. The spectra are interpreted using a bottom-up approach, where the complexity of the spin system is increased to match the experimental data.

On the other hand, spectra of MNP are interpreted using a top-down approach – which starts from the properties of the bulk material, and then decreases the volume of the bulk material until the simulations match the spectra.

A Spin Hamiltonian model that is often used in the analysis of MNP is the Giant Spin Hamiltonian (GSH) model [11–13]. The GSH is based on the assumption that the lowest spin multiplet of the molecule is sufficiently separated in energy from the other spin multiplets. This allows for the magnetic properties of the particle to be described by a single, giant, spin ground state [21]. Therefore, the anisotropies in the signal are interpreted by this model based on the ground state of a giant spin, rather than from the coupling of localized spin moments – which is the case in the interpretation of MNM, which form much smaller spin systems.

The total ground spin state of a system, indicative of whether the sample is a MNM or a MNP, can be approximated as

$$S = \mu / g\mu_B, \tag{2.7}$$

with μ the magnetic moment of the particle. The magnetic moment is defined, in this context, as

$$\mu = M_s V, \tag{2.8}$$

with M_s the saturation magnetization and V the volume of the particle. As can be seen in figure 2.3b, a large spin system results in a broad EPR spectrum.

In the following sections the approaches to analyse MNP and MNM systems are described, as discussed in [11]. In [7, 13] it is described how the spectra of MNP can be analysed using a simplified GSH. In this Spin Hamiltonian not the total ground spin state of the system is used in the Spin Hamiltonian, but rather an effective spin. This allows the analysis of MNP to be done using the quantum mechanical approach generally used when considering MNM. By scaling the spin used in the analysis, also the ZFS and temperature components described in Section 2.2.1 are scaled, and are therefore considered as effective terms.

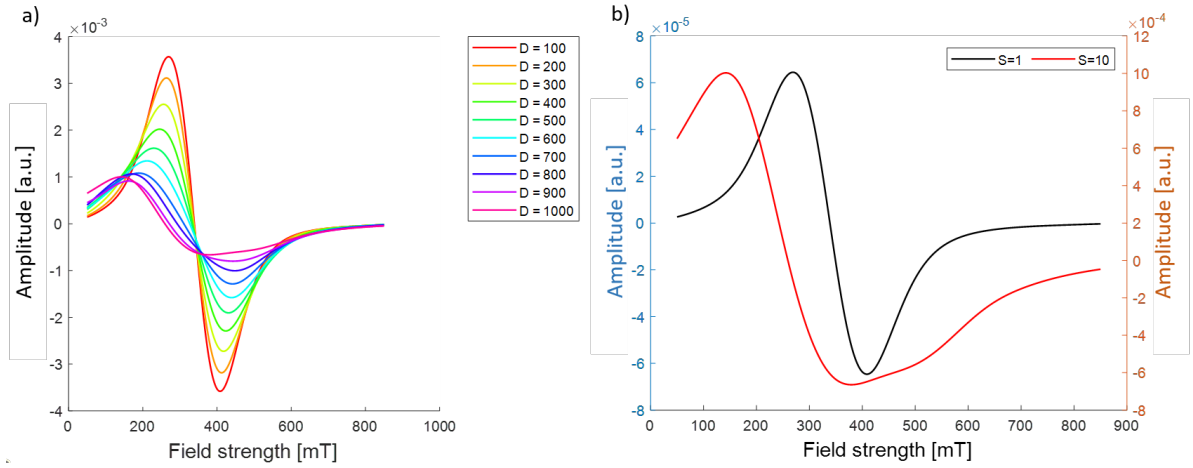

Figure 2.3: Simulations showing the effect of axial ZFS D and system spin S on lineshape. a): Simulations of varying axial ZFS D - in MHz - for a spin system with S=10 and isotropic g=2. b): Varying total spin S for axial ZFS D=1000 MHz. black: S=1; red: S=10. For both a) and b) the phenomenological linewidth peak-to-peak (lwpp) was a mix of two components: 100 mT Gaussian and 60 mT Lorentzian. This lwpp was used in order to show the global changes of the signal under the influence of a changing D ($E = 0$).

2.2.1. Resonance field analysis of MNM: the quantum mechanics approach

Here, the approach generally used to describe the temperature dependence of MNM is discussed. This system can also be used to discuss MNP when an effectively small spin system is considered. In the context of MNM, a relation exists between the axial ZFS component D and the anisotropy field (B_A) of a system. This relation is defined as

$$D = -\frac{B_A}{2S}. \tag{2.9}$$

The anisotropy field describes how much field strength needs to be applied to reverse the spin away from its easy-axis direction. For an uniaxial system the saturated magnetization is aligned along the axis of the effective magnetic anisotropy K. Given that the anisotropy field can be determined by equating B_A to $2KV/\mu$, with μ defined in equation 2.8, B_A can also be written as $2K/M_s$. The magnitude of M_s depends on the magnetic order of the system ground state and the measurement temperature considered. Assuming K to

be positive, D increases in magnitude with decreasing temperature when M_s decreases with temperature - such as in systems transitioning from SPM to AFM. The centres of the spectra - the resonance field B_{res} - are therefore expected to shift to lower fields under the conditions used in figure 2.3a. When the axial ZFS D is varied between 100 and 1000 MHz for an isotropic spin S=10 system, with g=2 and E=0 MHz, the resonance field decreases.

This shift of the resonance field is analytically described under the strong field approximation ($B_0 >> B_A$) and for a transition of a single spin state Δm_s using the following equation [7]:

$$B_{res} = B_0 + \frac{D}{2g_e\mu_B}(2s-1)(3cos^2(\theta)-1). \tag{2.10}$$

In equation 2.10 $D < 0$, B_0 is the resonance field of the free electron, and θ is defined as the angle between the applied field and the anisotropy axis. Apart from a shift in resonance field with increasing $|D|$ also the spectrum broadens, due to the increasing anisotropy of the system, and the signal amplitude of the spectrum decreases.

2.2.2. Resonance field analysis of MNP: the classical mechanics approach

Here, the approach used to describe the temperature dependence of MNP is discussed. The thermal behaviour of B_{res} of uniaxial MNP under the strong field approximation is expressed as [7]:

$$B_{res} = B_0 - \frac{B_A}{2}\frac{L_2(x)}{L_1(x)}(3cos^2(\theta)-1). \tag{2.11}$$

In equation 2.11 $L_2(x) = 1-(3/x)L_1(x)$, with $L_1(x) = coth(x)-(1/x)$ the Langevin function and $x = \mu B/k_BT$. k_B is the Boltzmann constant. As in equation 2.10, θ is defined as the angle between the applied field B and the anisotropy axis and B_0 as the resonance field of the free electron. Under the condition that $\mu B << k_BT$, the Langevin functions working on the anisotropy field B_A induce a decrease of the resonance field with decreasing temperature. This is similar to what was shown in figure 2.3a, where B_{res} shifted to lower fields with increasing D.

Therefore, both the classical approach and the quantum mechanics approach describe the same trend of B_{res} with temperature.

3

Materials and methods

3.1. EPR samples: specifications and preparation

3.1.1. Sample specifications

Horse spleen ferritin Horse spleen ferritin was purchased from Sigma-Aldrich (product number: F4503). The ferritin concentration was 60 mg of protein/ml. The ferritin was stored in a saline solution buffer. The sample solution was clear and dark brown-red. The shell composition H/L subunit ratio was approximately 15/85 for HoSF [3, 22].

Human liver ferritin Human liver ferritin was purchased from LEE Biosolutions (#270-40). The ferritin was stored in a solution in tris-buffered sodium chloride (pH of 7.5), with bromo-nitro-dioxane and methylisothiazolone as preservatives. The sample solution was clear and reddish-brown, had a protein concentration of 4.5 mg/mL (studied by LEE Biosolutions using Lowry protein assay), and a purity of ≥ 95% (studied by LEE Biosolutions using SDS-PAGE).

Buffer used for background measurement HuLiFt The buffer solution was composed of 0.15 M NaCl and 10 mM Tris, pH 8.0. Of the solution, 0.1% of the volume was sodium azide.

3.1.2. Sample preparation

Horse spleen ferritin The ferritin solution, as obtained from the producer, was directly pipetted into a 4 mm suprasil quartz tube and frozen in liquid nitrogen. No air bubbles were trapped in the solution.

Human liver ferritin EPR sample tubes were prepared using the following procedure. Ferritin solution was dissolved in glycerol, such that the ferritin:glycerol volume ratio was 4:1. The solution was then pipetted with a glass Pasteur pipette into a quartz tube with an external diameter of 3 mm, making sure that there were no bubbles in the resulting solution. The tube was stored in a liquid nitrogen container until used for measurement.

3.2. EPR measurement conditions

Continuous-wave EPR spectra of the HuLiFt and buffer were recorded using a 9 GHz ELEXSYS E680 EPR spectrometer (Bruker, Rheinstetten, Germany), equipped with a rectangular cavity (ER 4102ST). The measurements were performed at various temperatures, under the following conditions: 2.946 mT of modulation amplitude, 10 dB of attenuation (i.e. 20 mW) and 90 kHz modulation frequency. Each measurement was the average of eight scans, acquired in a field range of 50-850 mT. Accumulation time per spectrum was 11.2 minutes.

For a description of the full measurement procedure and the temperature regulation parameters, see Appendix A. All HuLiFt and buffer spectra discussed were measured by me and J. A. Labra-Muñoz. Due to the access restrictions to the laboratory only the temperatures discussed in this thesis could be acquired.

3.3. Data pre-processing procedure

The HoSF spectra were provided during the pandemic lockdown for the sake of developing the analytical approach discussed below. Many assumptions used in the analysis of the HuLiFt are therefore based on the early analysis of the HoSF spectra provided. Please note that the acquisition parameters for the HoSF sample were optimized for a different study.

The pre-processing procedure is summarised in figure 3.1.The spectra were background- and baseline-corrected, as described in Section 3.3.1. The methods used were different for HuLiFt spectra than for HoSF spectra. The feature at g'=4.3 was fitted and simulated as described in Section 3.3.2. In this section is also described how the signals centred around g'≈2 were isolated. The broad component of the remaining signal is that of the ferritin core, and is henceforth referred to as the ferritin-core signal. In Section 3.4 the conditions are discussed on which the analyses of the ferritin-core signal are based.

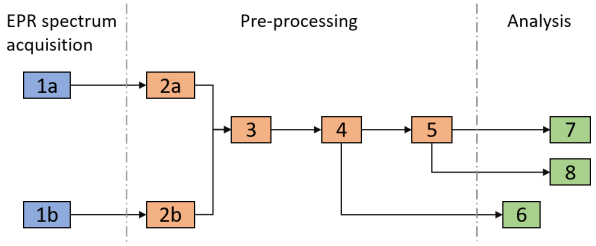

Figure 3.1: Pre-processing and analysis pipeline of the acquired spectra. 1: acquired ferritin (a) and buffer (b) data in .DSC format; 2: .DSC files converted to .mat format for processing in Matlab; 3: background correction; 4: baseline-correction; 5: ferritin-core signal isolation; 6: g'=4.3 simulation; 7: phenomenological analysis; 8: Easyspin analysis.

3.3.1. Background and linear baseline correction

All raw spectra were baseline-corrected, as on visual inspection there was a linear background signal perturbing the signal of interest. The approach used for the HoSF and HuLiFt spectra was different, since for HoSF no background measurements were available and the signal intensity of the HoSF was significantly higher than for HuLiFt. This difference in signal intensity meant that the contribution of the background to the measured sample signal is much smaller for the HoSF than for the HuLiFt, and the lack of the background measurements therefore acceptable for the current purpose. Furthermore, the signal of the HoSF disappeared between 20 and 30 K, indicating that between these temperatures the spins were fully blocked [20], and the slope - the baseline - of the spectra was otherwise fairly consistent between different temperatures.

On the other hand, the signal of the raw HuLiFt spectra had, due to the contribution of the background signal to the overall signal, a strong baseline that was dependent both on the acquisition temperature and the temperature-stabilization time.

HoSF For the HoSF, no spectra of background measurements were provided. As the signal was linear and flat at 10 and 20 K, it was assumed that minor background-corrections of all temperatures in the dataset could be performed based on a linear fit including data obtained in the field ranges 50-65 and 420-900 mT. These field ranges were considered, as the signal was flat at these fields in the 10 and 20 K spectra, and the second derivative of the respective absorption spectra were constant.

Based on this approach, all HoSF spectra were baseline-corrected by subtracting a linear fit with the slope and offset obtained from the 10 K spectrum: slope = -0.0023; offset = -1.6306. The resulting spectra are shown in figure B.1a, and zoomed in on the lineshape of the ferritin-core signal in figure B.1b.

HuLiFt For the HuLiFt we measured both the sample and the buffer under identical conditions. Background-correction was performed by subtracting the buffer spectra from the sample spectra. The baseline was removed by including a linear term to the Gaussian function used to fit the spectra, which was defined as

$$\texttt{phenomenological fit}(\mu_G,\sigma,A,a,b,x) = A\cdot\frac{-1}{\sqrt{2\pi}}\cdot e^{-(x-\mu_G)^2/2\sigma^2}\cdot\frac{x-\mu_G}{\sigma^2}+ax+b, \tag{3.1}$$

and subtracting the linear component of the fit - $ax+b$ - from the data. An example of the linear background correction procedure is shown in figure 3.2 for the HuLiFt spectra measured at 20 K. This approach was used as the absorption band of the sample, of which the EPR signal is the derivative, was well captured

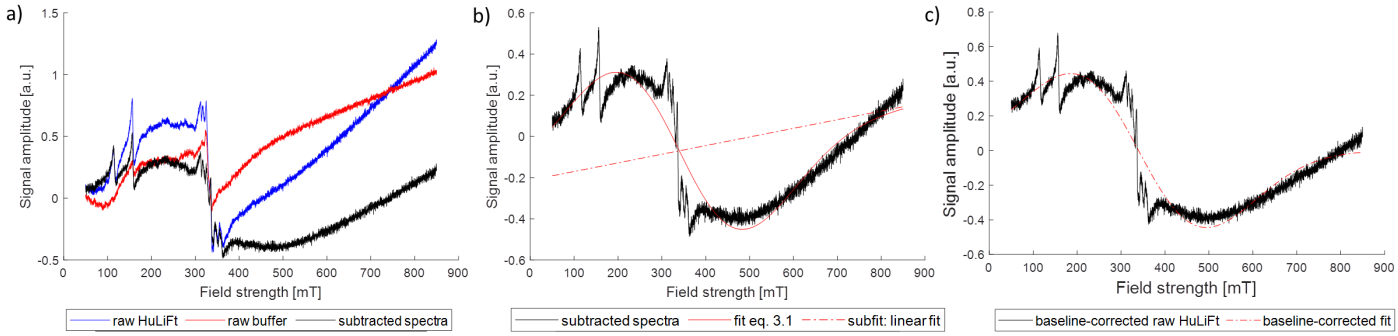

Figure 3.2: Background correction procedure as performed on HuLiFt (20 K). a): blue: raw HuLiFt sample spectrum; red: raw buffer spectrum; black: background-corrected HuLiFt spectrum. b): black: background-corrected HuLiFt spectrum; solid red: fit from equation 3.1; dashed red: linear component of fit. c): black: baseline-corrected HuLiFt spectrum; bashed red: baseline-corrected fit.

by a Gaussian distribution. The background was assumed to contribute a linear trend to the measured signal, according to the whole field range.

In equation 3.1, μ_G is the mean of the Gaussian and σ the standard deviation, indicating the separation between the mean and the peaks, while x is the applied field. A is the scaling factor needed to relate the amplitude from the otherwise normalised Gaussian derivative to the signal amplitude of the spectra. The slope and offset considered in the fit are defined as a and b, respectively.

The fitting parameters were initialised as: μ_G = 300 mT (ranging from 300 to 400 mT); σ = 200 mT (ranging from 40 to 200 mT); A = 3 (ranging from -3 to 900); a = 2 (ranging from -2 to 2); and b = -1 (ranging from -1 to 1). These initial fitting parameters and ranges were used for each temperature, and fitting was performed using the `fit` function - operating the nonlinear least-square fit algorithm - in Matlab, allowing for the determination of the quality of each fit and the standard error on each of the fitting parameters.

3.3.2. Isolating the ferritin-core signal around g'≈2

Extraction of the Fe^{3+} signal: simulation In order to isolate the ferritin-core signal around g'≈2, the feature at g'=4.3 - centred around 158 mT in the HoSF spectrum shown in figure B.1, and zoomed in on in figure 3.3a - needed to be extracted. This feature belongs to aspecific Fe^{3+} sites, as will be discussed later. Extraction of this feature was done by fitting solely the feature in the field range 120-210 mT of the HoSF spectra using EasySpin. The fit was based on equations 2.2 and 2.3. The parameters required were the total spin S, a rhombic g-tensor and both the axial and rhombic ZFS terms. Furthermore, a gStrain, describing a distribution in g values, was added. Following a similar approach as in [20], the parameters were optimized for the signal at 20 K through manual parameter variation and least-squares fitting (Nelder/Mead simplex). The optimized parameters, yielding a root-mean-square error of less than 2.5%, are summarized in table 3.1 and successfully described this feature at higher temperatures as well.

Table 3.1: Fitting parameters used to describe the signal at g'=4.3, belonging to Fe^{3+} sites in the HoSF and HuLiFt spectra.

Fe^{3+}	**S**	**D (MHz)**	**|E/D|**	$\mathbf{g}_x$	$\mathbf{g}_y$	$\mathbf{g}_z$	$\mathbf{gStrain}_x$	$\mathbf{gStrain}_y$	$\mathbf{gStrain}_z$
	5/2	20960	0.3324	1.6807	1.99232	2.00548	0.799637	0.136306	0.0262458

In figures 3.3a,b, the feature in the HoSF spectra at 20 and 231 K is shown in black, overlayed by the simulation after fitting in red. The difference between spectra and simulations is shown in blue. Furthermore, these parameters were also appropriate for the description of the g'=4.3 feature in the HuLiFt spectra, as can be seen in figure 3.3c for the signal at 20 K.

Removal of unwanted features: HSVD As can be seen in figure 3.3, subtraction of the simulation from the data generates artefacts, due to the signal-to-noise ratio (SNR) of the spectra and the fit performance for each respective temperature. Furthermore, as can be seen in figure 3.2 and is indicated in figure 3.4, the HuLiFt spectra contain additional features at g'=5.85 (centred around 116 mT) and around g'≈2 (a six-line signal ranging between 308 and 364 mT), which further obscure the ferritin-core signal. In order to isolate the signals around g'≈2, a Hankel singular value decomposition algorithm was applied. The algorithm will

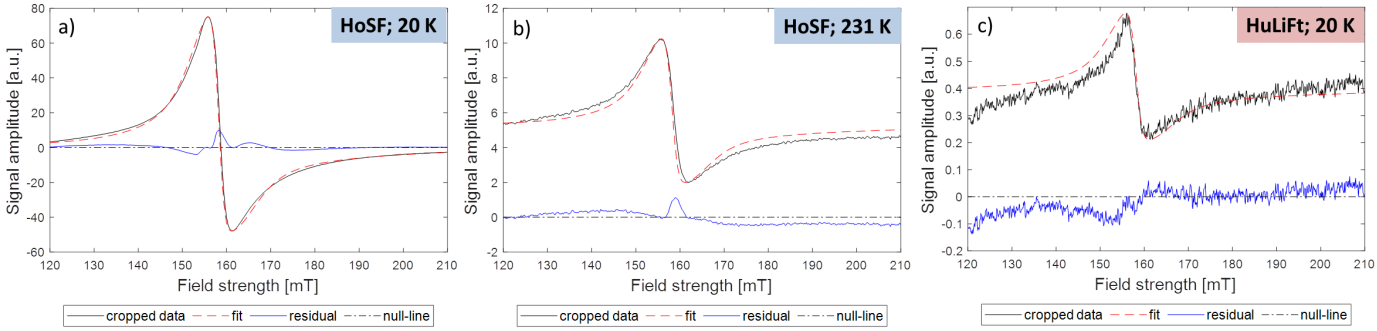

Figure 3.3: Simulation of signal of aspecific Fe^{3+} sites in HoSF (a: 20 K, b: 231 K) and HuLiFt (c: 20 K), using the parameters in table 3.1. solid black: experimental data; red: simulation; blue: residuals; dashed black: null-line for amplitude reference.

be referred to as HSVD, and is used in the field of nuclear magnetic resonance and magnetic resonance spectroscopy, aiding in the analysis of structured and complex data. The algorithm used was created based on [17, 34] and the Matlab implementation was provided by Dr. I. Ronen from the Leiden University Medical Centre.

Since CW-EPR data is not complex, the data was treated such as to create both an imaginary and a real component, with the former set to zero. This allowed for the application of the HSVD algorithm. The algorithm decomposes a spectrum in the Fourier conjugate domain, and the resulting signal is treated as a summation of decaying exponentials with given amplitude, phase, decay rate and frequency. This results in an approximation of the spectra as a summation of Lorentzian lineshapes, which are fitted and later subtracted from the data. The goal was to eliminate the features at g'=4.3 and g'=5.85.

The optimal parameters of the HSVD were found through trial and error. For the reconstruction of the signal, 1/32nd of the data in Fourier domain was therefore used to predict the next 1/32nd of the spectrum (FID=32), until the full signal was reconstructed. A maximum of 60 components (rank=60) was allowed for the reconstruction.

The closeness of approximation was estimated based on the residuals between the spectrum and the summation of Lorentzian lineshapes, an example of which is shown in figure 3.4a for a HuLiFt spectrum, and through visual inspection. The HSVD-treated data had to be rescaled and offset corrected to compensate for the loss in intensity caused by the data conversion. In figure 3.4b the HSVD-treated HuLiFt spectrum at 5 K

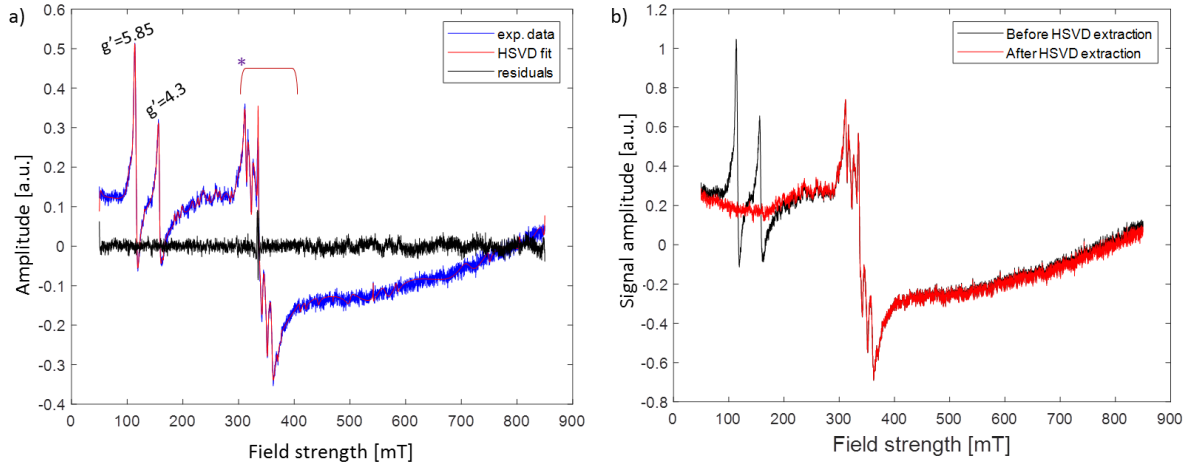

Figure 3.4: a) Example of a HuLiFt spectrum (5 K) fitted using the HSVD-procedure under the conditions: FID=32; rank=60. blue: baseline-corrected spectrum; red: HSVD reconstructed fit; black: residuals (spectrum - fit). Also indicated are the unwanted features at g'=5.85, g'=4.3, and the six-line signal around g'≈2 (indicated with bracket+*). b) The HuLiFt spectrum before (black) and after (red) HSVD-treatment to remove the features at g'=5.85 and g'=4.3.

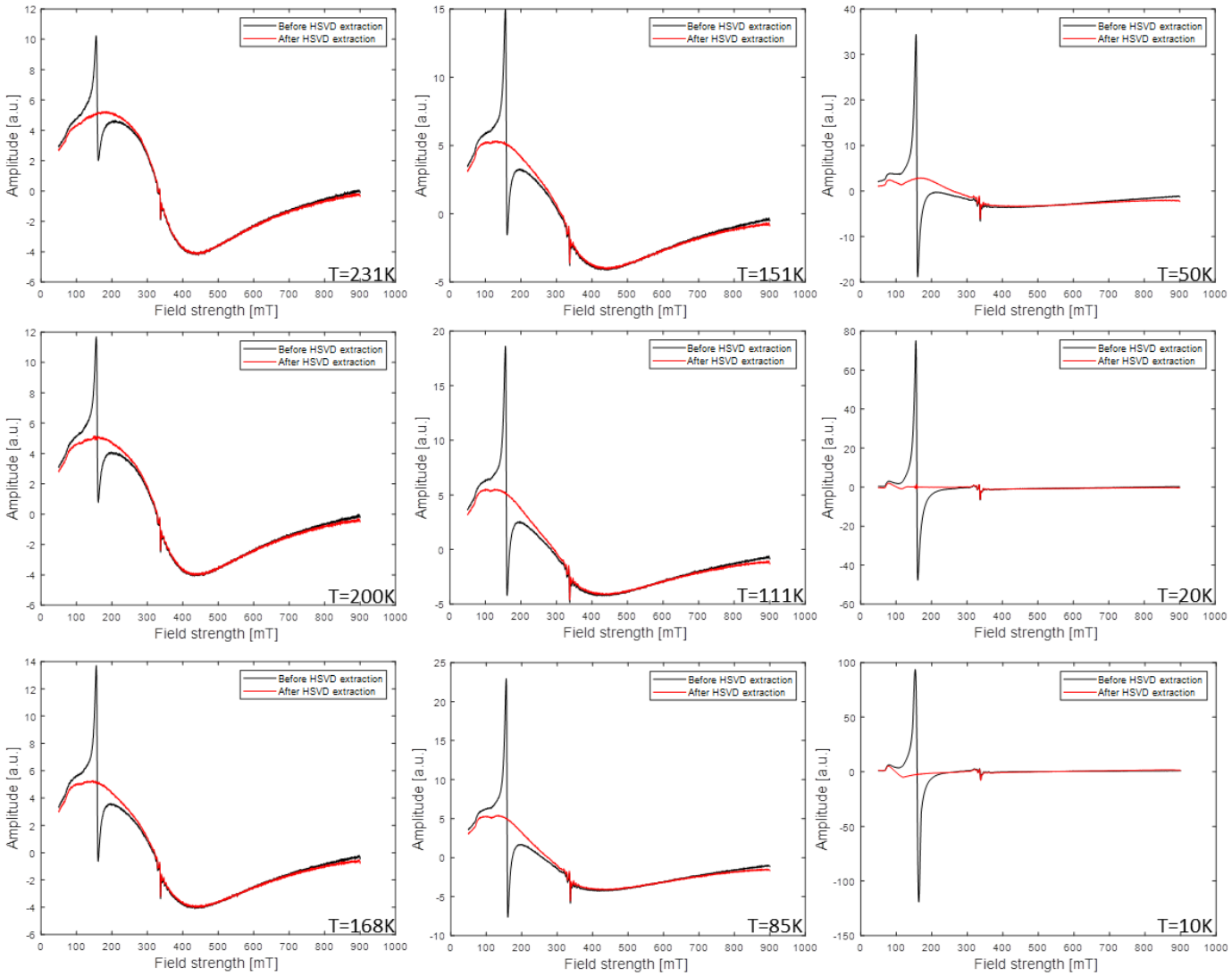

Figure 3.5: Baseline-corrected HoSF spectra before (in black) and after (in red) singular value decomposition (HSVD) treatment was applied to remove the signal composing the feature at g'=4.3.

is shown. In figure 3.5 the HoSF spectra before (in black) and after (in red) HSVD-treatment are shown for all considered temperatures, demonstrating the efficacy of this approach. For the HuLiFt spectra, the six-line signal around g'≈2 - indicated with bracket and star in figure 3.4a - could not be extracted, as this lead to distortions in the overall shape of the broad feature.

3.4. Modeling the ferritin-core signal at g'≈2

The ferritin-core signal was studied both by fitting the HSVD-treated data with equation 3.1, and by employing the Spin Hamiltonian approach using Easyspin. Both methods are described below.

3.4.1. Phenomenological analysis

From the fits performed with equation 3.1 the resonance field B_{res}, peak-to-peak amplitude A_{pp}, and resonance broadening ΔB_{pp} were obtained.

The resonance field B_{res} is the field strength that corresponds to the mean (μ_G) of the fit. The resonance broadening ΔB_{pp} is defined as 2σ, which corresponds with the field strengths at which the absolute minimum and maximum amplitudes of the fit occur. The sum of the absolute values of these amplitudes defines A_{pp}. Equation 3.1 contains both the Gaussian model used to approximate the lineshape and the linear background

correction. As the background was corrected in a previous pre-processing step, the linear component present in the analysis is negligible. The temperature dependence of the lineshape can in this manner be determined.

3.4.2. Easyspin analysis

For spectrum simulation and fitting with Easyspin a temperature dependent spin system of S=10 was assumed. The g-tensor was assumed isotropic and equal to 2.0154. Phenomenological linebroadening through the lwpp parameter was set to 90 mT. This parameter, which is composed of a Gaussian and a Lorentzian component, was allowed to vary with temperature. For the spectrum at 150 K, which can be described by a Lorentzian lineshape, lwpp was composed of a Gaussian linebroadening of 15 mT and a Lorentzian linebroadening of 75 mT. For all other temperatures, the phenomenological line broadening was Gaussian only. The ZFS parameter (**D**) was varied during the simulations and fits. Only axial D was considered, i.e. $D_z \neq 0$ and $D_x = D_y$. Furthermore, lineshape broadening using a strain on g was allowed. Solving the Spin Hamiltonian allows the determination of the Hamiltonian parameters that describe the magnetic structure of the ferritin core.

4

Results

The EPR spectra of HuLiFt measured at different temperatures are shown in figure 4.1. The ferritin-core signal is best seen in the spectrum acquired at 150 K, and it is broad with a ΔB_{pp} of ≈110 mT. The slope of the spectra varies widely and the signal amplitude is close to that of the background. In order to correct for the background signal present, the temperature dependence of the buffer was measured separately under the same conditions considered for the HuLiFt spectra.

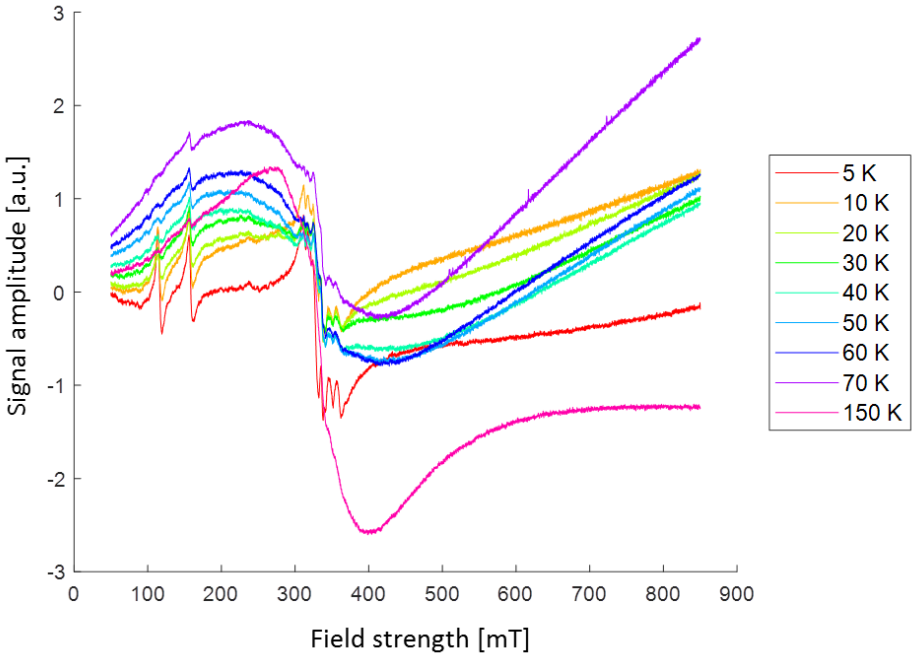

Figure 4.1: Raw spectra of HuLiFt sample acquired at different temperatures.

In order to correct for the baseline signal of the spectra, the slope and offset had to be determined for each spectrum. Typically, EPR spectra have linewidths between 0.1 and 1 mT. This is much narrower than the ferritin-core signal. For typical EPR spectra a linear interpolation of the low and high fields of the spectra is sufficient to determine the baseline, as the absorption spectra - the first integral of the EPR spectra - start and end at zero amplitude.

For HuLiFt spectra, however, this is not the case, as the linewidth is large and the signal amplitude at low-field (around 50 mT) and high-field (around 850 mT) does not decay to zero. Therefore, the procedure described in Section 3.3.1 was developed to correct for the baseline. Application hereof resulted in the spectra shown in figures 4.2a - where the spectrum for each temperature is shown separately - and 4.2b - where all spectra are overlapped.

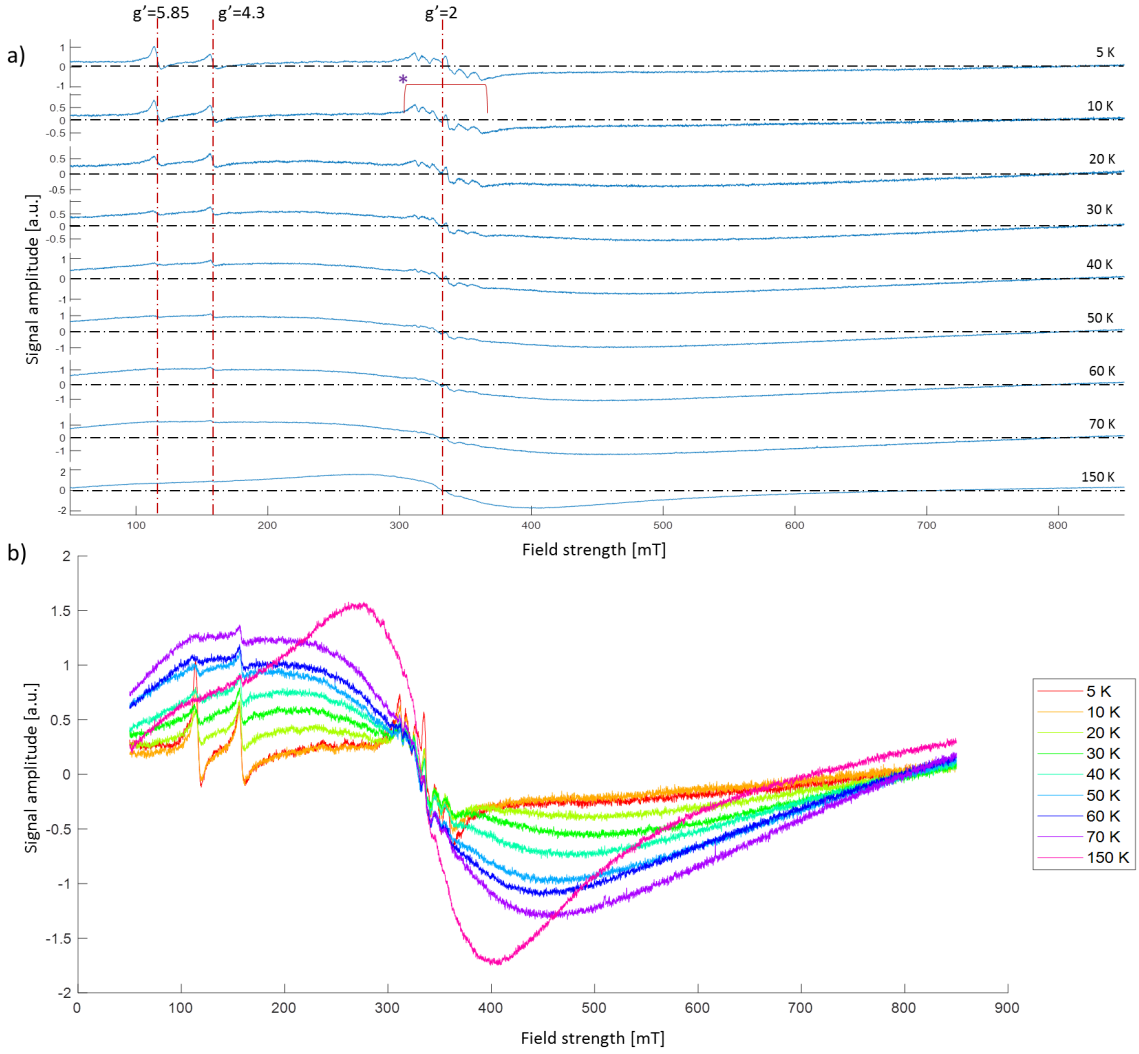

Figure 4.2: Baseline-corrected 9 GHz EPR spectra of HuLiFt acquired at different temperatures. The microwave frequency was 9.49 GHz, acquired in field range 50-850 mT. In a) the main features around g'=4.3 (rhombic Fe^{3+} sites), g'=5.85 and g'=2 (*: six-line signal; broad signal: mineral core of ferritin) are indicated. In b) all overlayed spectra presented, showing the evolution of the lineshape of the broad signal under the influence of the temperature.

In the spectra shown in figure 4.2a, the ferritin-core signal is now clearly visible. The spectra contain a narrow feature at g'=5.85, a six-line signal around g'≈2 - indicated with a bracket and a star -, a broad signal around g'≈2 - the ferritin-core signal - and a narrow feature at g'=4.3.

Inspection by eye of the ferritin-core spectra in figure 4.2 shows that the field strength at which the spectrum crosses zero - the resonance field B_{res} - is obscured by the six-line signal. This makes it difficult to determine how B_{res} changes with temperature. For the 20 to 70 K spectra, ΔB_{pp} appears to be around 300 mT, but this is difficult to assess, as the low-field peak of the ferritin-core signal at these temperatures is partially obscured by the narrow features at g'=5.85 and g'=4.3. The shape of the spectrum measured at 150 K differs from the other spectra. It is least obscured by the features present at the lower temperatures, has a reduced ΔB_{pp} of approximately 110 mT centred around g'≈2, and a shoulder structure in the range 50-200 mT.

In order to better determine the evolution of the ferritin-core signal with temperature, the features at g'=5.85 and g'=4.3 were removed using the HSVD procedure described in Section 3.3.2. The resulting spectra are shown in red in figure 4.3. These spectra were fitted in the analyses described in the following sections.

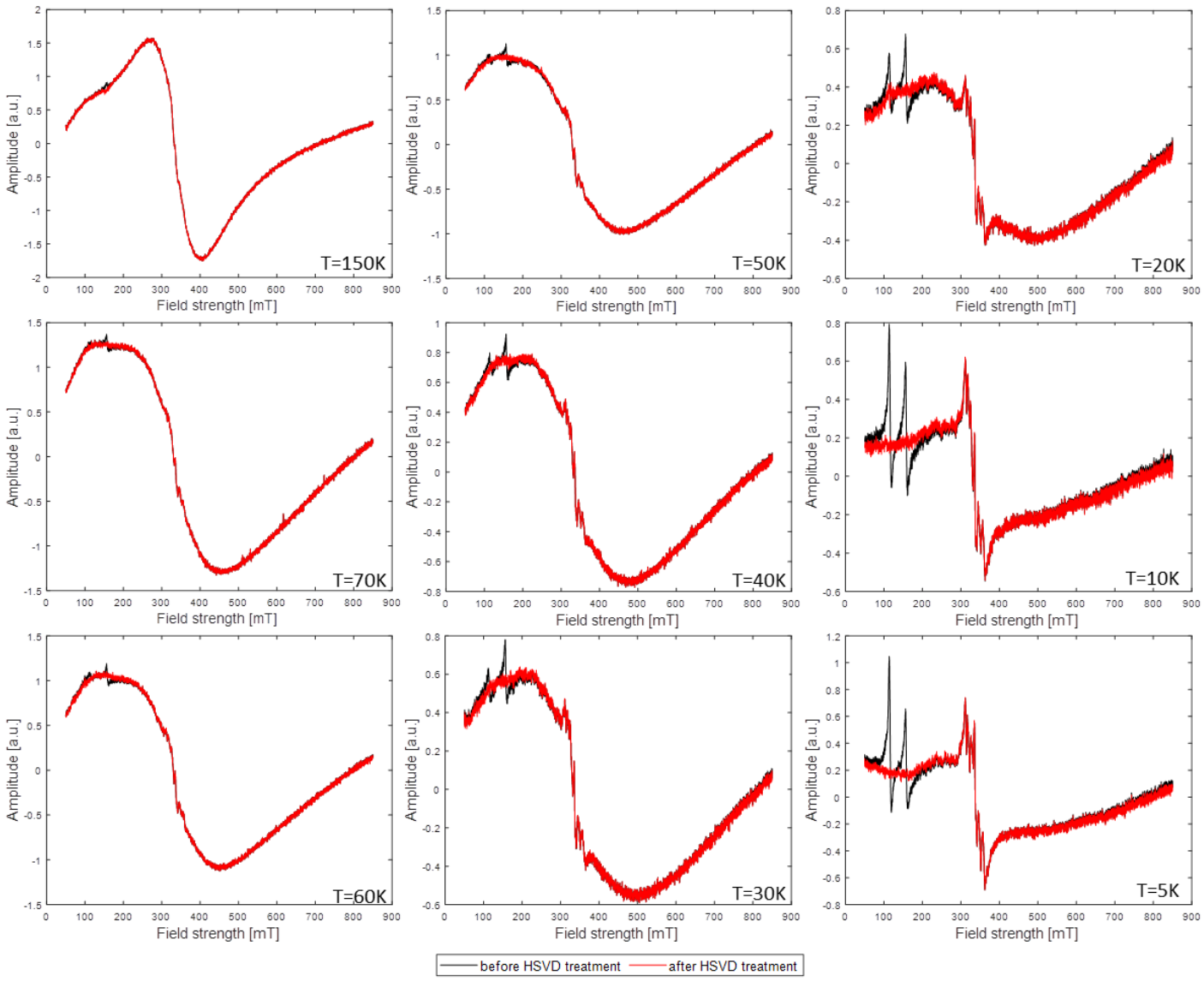

Figure 4.3: Baseline-corrected HuLiFt spectra before (in black) and after (in red) singular value decomposition (HSVD) treatment was applied to remove the signals composing the features at g'=4.3 and g'=5.85.

4.1. Phenomenological analysis

The HSVD-treated spectra were fitted using equation 3.1. The baseline component of this fit was negligible since the data was baseline-corrected with the same equation prior to HSVD-treatment. The resulting Gaussian derivative fits are shown in red in figure 4.4, overlapping the spectra prior to HSVD-treatment. The null-line is indicated as a reference.

The fits in figure 4.4 show that the Gaussian derivative describes the spectra acquired between 20 and 70 K well for the low-field peak half of the ferritin-core signal. The high-field peak half of the ferritin-core signal deviates more strongly from the Gaussian. As can be seen in figure 4.5, the 150 K spectrum is described better by a Lorentzian derivative than by a Gaussian derivative. For the 5 and 10 K spectra the signal could not be fitted well by either model, due to the intensity of the six-line signal. Additionally, at these temperatures no signal corresponding to the ferritin-core signal described above is observed.

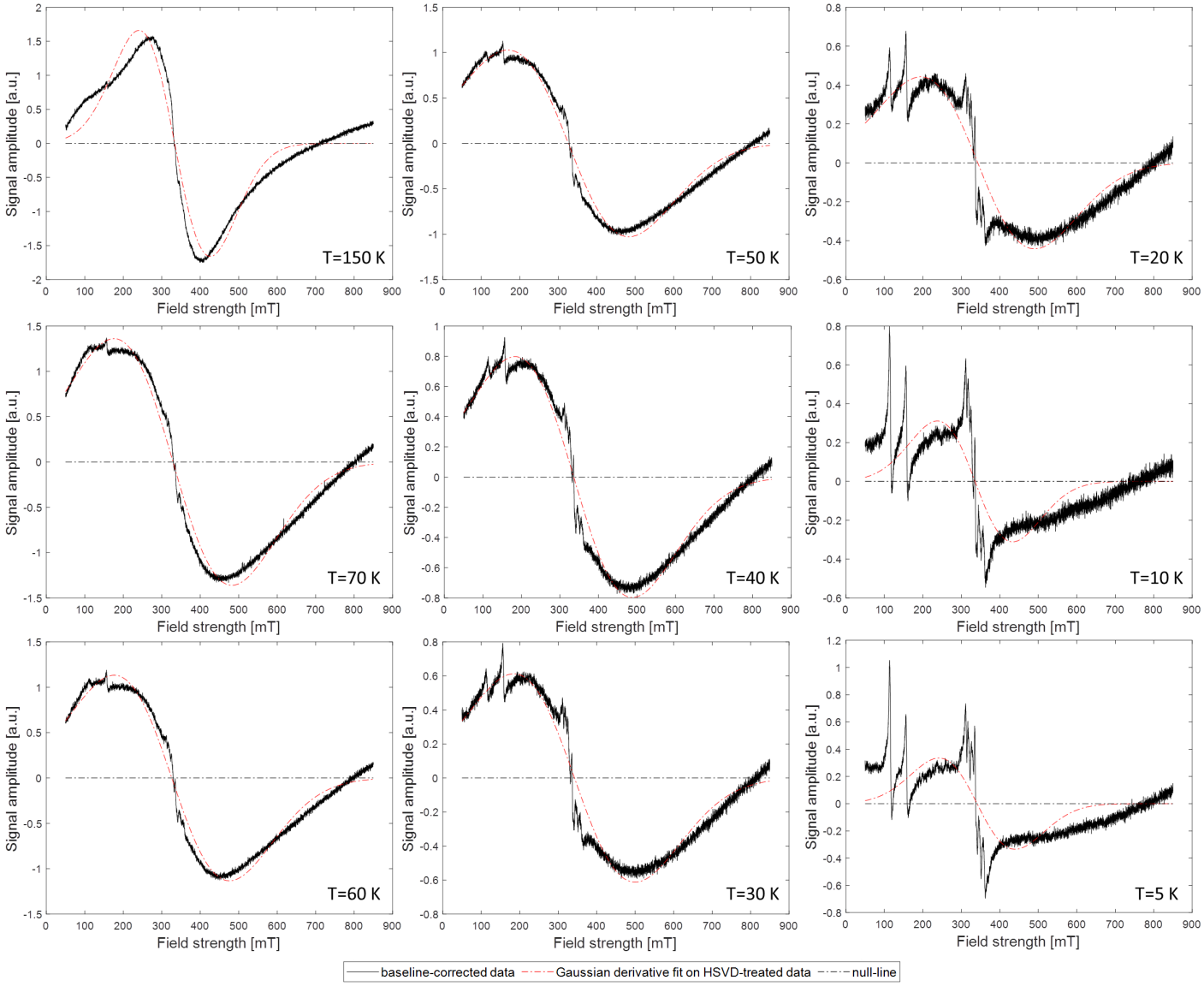

Figure 4.4: Phenomenological analysis of HSVD-treated HuLiFt spectra using equation 3.1. black: Baseline-corrected HuLiFt data before HSVD-treatment; red: Gaussian fit of HSVD-treated HuLiFt data; dashed black: null-line.

As can be seen in figure 4.5, the 150 K spectrum was better described by a Lorentzian derivative function. Despite this, all spectra were described by Gaussian functions in figure 4.4 in order to allow comparison of similarly acquired fitting parameters. From each Gaussian fit the resonance field B_{res}, resonance broadening ΔB_{pp} and peak-to-peak amplitude A_{pp} were obtained. The magnitude of these parameters with respect to

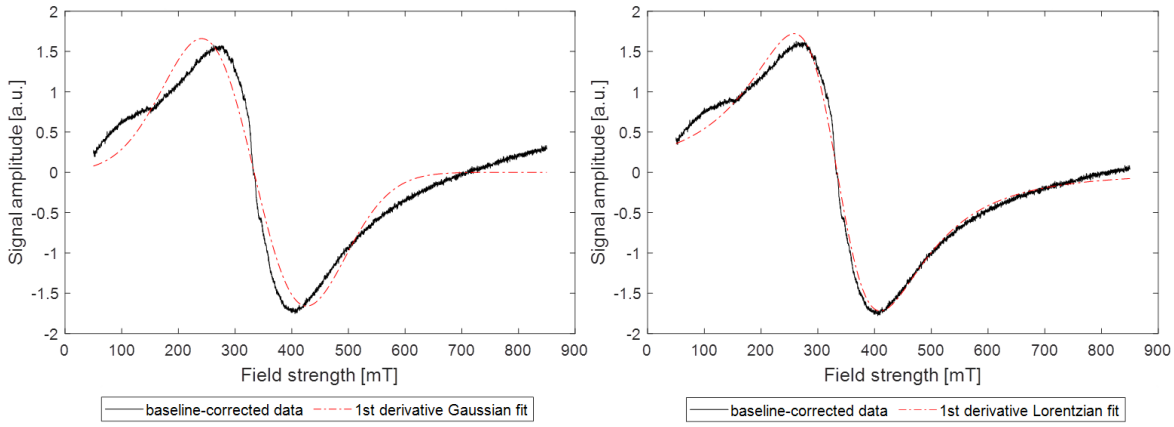

Figure 4.5: Comparison of the performance of Gaussian and Lorentzian derivative models (in red) used to baseline-correct and fit the HSVD-treated HuLiFt spectrum (in black) acquired at 150 K.

temperature is plotted in figure 4.6. Details to those parameters are given in Section 3.4.1.

Figure 4.6a shows that B_{res} does not change much with temperature, remaining between 328 and 342 mT for all temperatures. ΔB_{pp} likewise remains relatively constant between 297 and 315 mT, at temperatures from 20 to 70 K. At 150 K ΔB_{pp} drops to 185 mT, which reflects the narrowing lineshape observed in figure 4.2 well. Figure 4.6b shows that the peak-to-peak amplitude A_{pp} increases linearly with temperature between 20 and 70 K. The data below 20 K were not included in the analysis due to the poor fit performance. The datapoint at 150 K deviates from the fit, suggesting a change in the trend of the parameter.

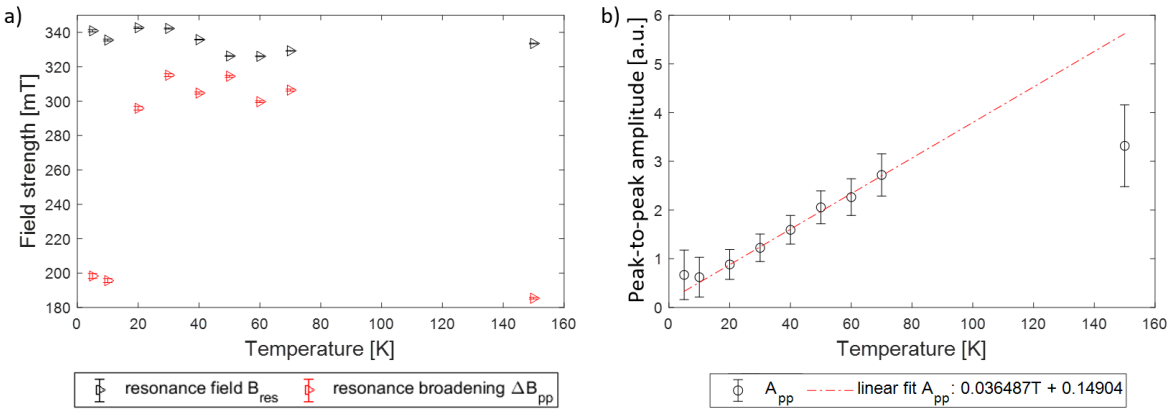

Figure 4.6: a) Temperature dependence of the fitted resonance parameters: resonance field B_{res} (black) and resonance broadening ΔB_{pp} (red). b) Temperature dependence of the peak-to-peak amplitude A_{pp}. The linear fit is based on the data between 20 and 70 K. Error bars represent the 95% confidence bounds of the fits.

4.2. Easyspin analysis

Of all ferritin-core spectra in the considered temperature range, the 150 K spectrum is the most structured. It has a shoulder structure between 50 and 200 mT and a distinct Lorentzian lineshape. This spectrum was therefore selected for analysis with Easyspin. The spectrum was both simulated and fitted, considering a total spin S of 10. The remaining parameters are given in Section 3.4.2. The axial ZFS D and gStrain parameters were left to vary.

Simulations of D varying between 340 and 380 MHz, in the absence of gStrain are shown in figure 4.7a. They show that the chosen range of D in this range was able to describe the position of the ferritin-core signal well. However, the shape of the spectra, in particular the shoulder structure between 50 and 200 mT and the broadening at higher fields, was not well captured. Values of D outside this range provided shifted spectra that disagree with the centre of the resonance observed. As shown in figure 4.7b for D equal to 350 MHz, the shoulder structure between 50 and 200 mT and the higher field broadening could not be described by the

inclusion of a (large) gStrain. Allowing D and gStrain to vary simultaneously between the boundaries set in figures 4.7a,b resulted in figure 4.7c. It shows that, although the main feature is captured, it is not possible to get a complete agreement between the considered model, using a single D parameter, and the experimental data. This indicates that the model of a single D parameter does not agree well with the experimental data. Possible alternatives are described in Section 5.

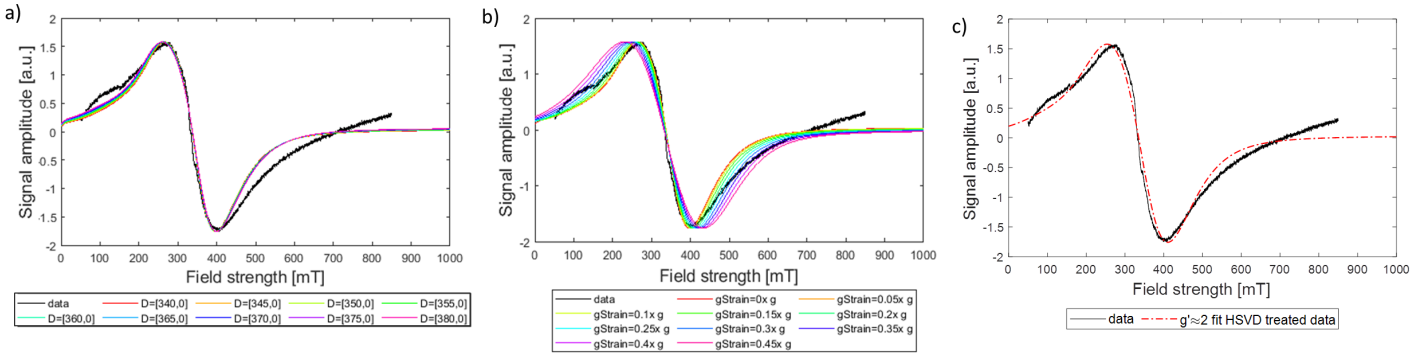

Figure 4.7: Simulations of the effect of D a) in a small range around its optimum, and gStrain b), performed separately on the HSVD treated HuLiFt spectrum acquired at 150 K. c) Nelder/Mead fit with D and gStrain varying in the ranges as defined in a) and b). black: HSVD-treated spectrum; red: optimal fit. Simulations and fits were performed in the field range 0-1000 mT. Broadening of the line-shape for both simulations and fits was performed using a combination of 15 mT Gaussian lineshape broadening and 75 mT Lorentzian lineshape broadening.

Even though a good Spin Hamiltonian description could not be found within the timeframe of this thesis, a method was designed by which such a model could be applied to a temperature series of spectra including automized fitting. The pre-processing steps applied to each spectrum are as described in Sections 3.3.1-HuLiFt and 3.3.2. The resulting spectra were fitted using EasySpin, as previously described for the 150 K spectrum and in Section 3.4.2.

Figure 4.8 shows that the method overall works well. The g'=4.3 feature is well described using the fit parameters given in table 3.1. Only the amplitude of the g'=4.3 feature at one temperature, 150 K, does not fit as well as the rest. Figure 4.8 shows that the automatic fitting procedure, applied to the spectra in the 10-150 K temperature range, works well. The method, therefore, is ready to be applied once a suitable model for D is found.

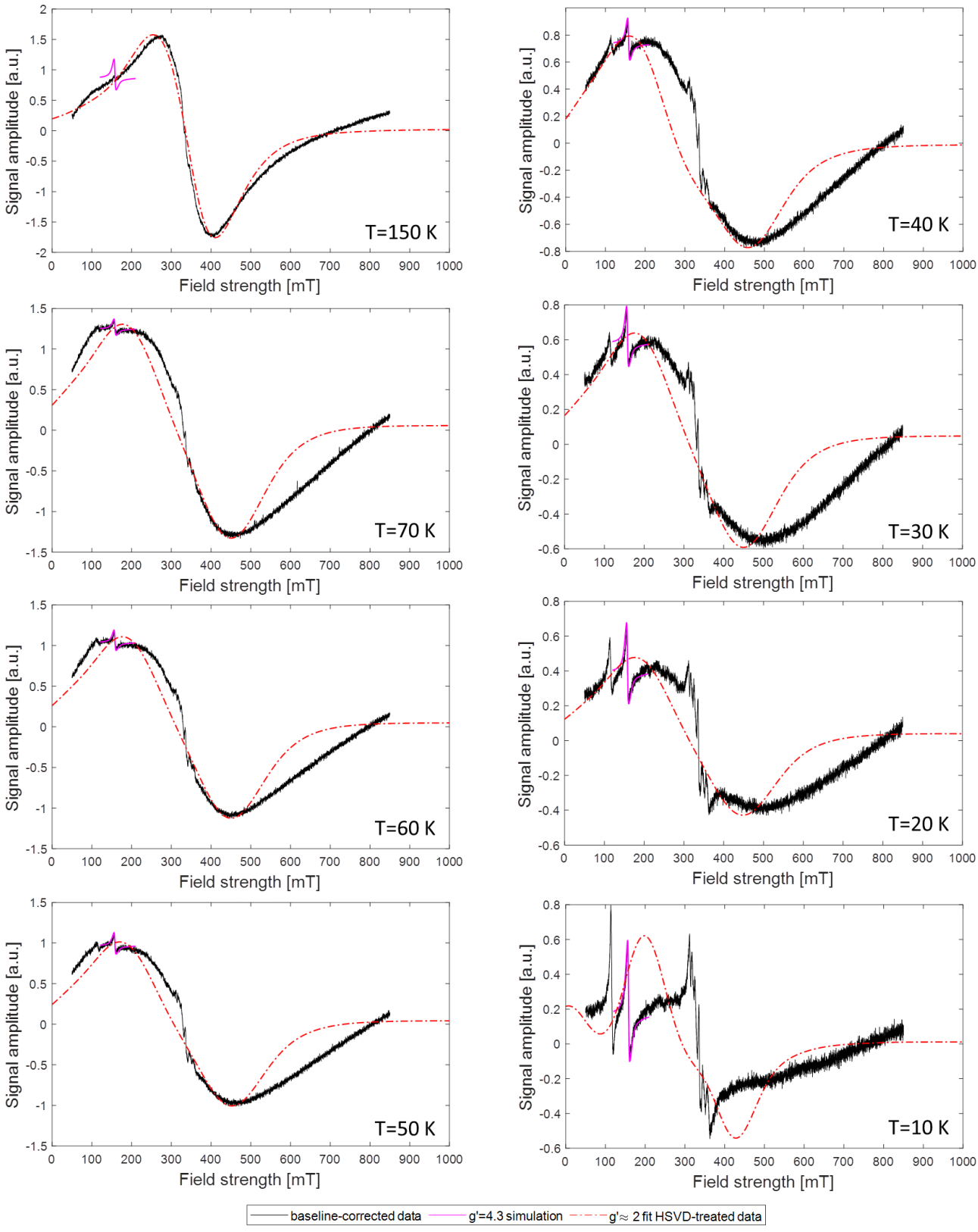

Figure 4.8: Fits of the ferritin-core signal (red, dashed) and simulations of the g'=4.3 feature (magenta) overlapping the baseline-corrected HuLiFt spectra before HSVD-treatment (black), acquired at temperatures 10 K - 150 K. Magenta: simulations performed in the field range 120-210 mT. Red, dashed: fits performed on the HSVD-treated spectra, in the field range 0-1000 mT. With the exception of the spectrum acquired at 150 K, all spectra were broadened using a Gaussian lwpp of 90 mT.

5

Discussion

5.1. Factors complicating the acquisition and analysis of ferritin-core EPR spectra

While commonly EPR spectra have a peak-to-peak linewidth of 0.1-1 mT, the ferritin-core signal is several hundreds of mT broad. This broadness makes measurement of these spectra less straightforward. One of the key parameters in the optimization of the signal amplitude is the modulation amplitude. The modulation amplitude is ideally chosen such that it is equal to a tenth of the true peak-to-peak linewidth of the signal. This linewidth is determined by acquiring the spectrum at several modulation amplitudes, and is considered "true" when it does not change with decreasing modulation amplitude. The ferritin spectrum would have required a modulation amplitude of at least 10 mT. However, the setup was limited to 3 mT, effectively reducing the signal amplitude by at least a factor of two. Because of this reason, combined with the low concentration of the HuLiFt sample, the signal amplitude is close to that of the background signal, as can be seen in figure 3.2a. Additionally, the signal extends beyond the measurement range.

These factors make that background- and baseline-corrections of the ferritin spectra are very challenging, and require ad-hoc solutions. Finally, the usage of a high modulation amplitude - although it has the advantage of increasing the signal amplitude - enhances unwanted background features, such as a linear slope in the baseline.

In addition to the experimental limitations, the ferritin spectra contain narrow signals, most likely of paramagnetic centres other than from the ferritin core, that hamper the analysis. This is clearly visible in figure 4.2a

5.2. Treatment of the baseline of the EPR spectra

The standard procedure for background and baseline correction entails performing a linear baseline correction on the sample and background spectra, and subtracting the resulting spectra from each other. These corrections are linear, and based on the spectral regions that contain no signal. However, as these regions were not present in the HuLiFt spectra, this procedure could not be used. Therefore, the background and baseline were addressed through a combination of buffer-signal subtraction and Gaussian derivative fit with linear baseline, as described in Section 3.3.1, using equation 3.1. This procedure worked well for the spectra acquired between 20 and 70 K, and allowed for the correction of the HuLiFt spectra shown in figure 4.1. The resulting spectra are shown in figure 4.2. As shown in figure 4.5 a Lorentzian derivative fit with linear baseline provides an overall better spectrum description for the 150 K dataset.

In order to improve the analysis of the ferritin signal, the narrow features obscuring the low-field peak – i.e. the features indicated at g'=5.85 and g'=4.3 in figure 4.2a – were removed using the HSVD-treatment described in 3.3.2. The HSVD-treatment preserved the general lineshape of the HuLiFt spectra well using the considered FID and rank parameters, which were empirically determined. As the residuals of HSVD-fits and data were small in amplitude, the ferritin-core signal was considered acceptably approximated after removal of the narrow features. The ferritin-core signal was assumed to not depend strongly on these features, which were Lorentzian in lineshape. Unfortunately, the six-line signal could not be removed using this approach, as it was not composed of Lorentzian lineshapes. The determination of the components required for the composition

of the unwanted features is dependent on the considered FID and rank parameters, and is performed for each spectrum separately. The resulting HSVD-treated HuLiFt spectra were shown in 4.3. The HSVD-treatment was additionally applied to the HoSF spectra, which were shown in figure 3.5. As can be seen, this technique works reliably for the removal of low and high signal amplitude features of Lorentzian lineshape.

5.3. Origin of the narrow features

Here, an attempt was made to explain the origin of the narrow features obscuring the ferritin-core signal – i.e. the features at g'=5.85, g'=4.3 and the six-line signal around g'≈2, as indicated in figure 4.2a. These signals increase in intensity as the temperature decreases, and are present even at 5 K, as shown in figure 3.4. At 150 K they are almost completely absent.

The feature at g'=4.3 was ascribed to Fe^{3+} sites of low symmetry, as this was the case for this feature in the HoSF spectra [20]. This feature is typically referred to in literature as "trash-iron", due to its common presence in biological samples and low specificity of binding site. The feature at g'=5.85 might belong to high-spin Fe^{3+} in methemoglobin, which has been shown to appear around g'=5.83 – g'=6 in native human blood [19]. Temperature behaviour of the g'=5.85 signal amplitude is similar to that detected with EPR for methemoglobin [30]. Methemoglobin is often accompanied by the presence of nitrite [30] or copper [18] complexes. These do not, however, appear to cause the six-line signal around g'≈2. Instead, this signal could be caused by the presence of manganese, which can often be found in minerals in combination with iron [27], and of which high concentrations can be found in the liver [9]. The six-line signal might therefore be the result of hyperfine interactions between the nuclear spin I of manganese and the electron spin S of the iron mineral complex. Previous temperature dependent EPR studies of manganese show a similar signal development with temperature [4, 15, 31] as perceived in the spectra presented in this thesis. Additionally, I acquired similar lineshapes by performing simulations around g'=2.0059 isotropic with a hyperfine coupling constant of 280 MHz in the description of hyperfine splitting between a ^{55}Mn nucleus and different spin systems (not included in this thesis). An EPR study of engineered ferritin nanocages [24] obtained similarly behaving spectra around g'≈2, and ascribed their six-line signal to Mn^{2+} impurities present even in the absence of iron loading, further strengthening our hypothesis.

An SDS-PAGE assay of the HuLiFt sample confirmed that the sample contained ≈95% ferritin, and excluded the presence of haemoglobin (private communication with Labra-Muñoz, J. A. & Ndamba, L.A.). Therefore, it is possible that other components than ferritin are also present in the sample.

5.4. Temperature dependence of the ferritin core EPR spectra

Evolution of the general lineshape At temperatures above 20 K, the signal amplitude of the ferritin-core signal increases with increasing temperature. This is opposite of what is expected from non-interacting unpaired spins, as is the case for the features at g'=5.85 and g'=4.3. Based on visual inspection of the HSVD-treated spectra, the high-field peak shifts to lower fields when temperature increases, suggesting either a change in the lineshape or a shift of the entire lineshape to lower fields with increasing temperature. Due to the position of the six-line signal, however, the overall trend of the lineshape is difficult to discern. Characterization of the overall lineshape changes was therefore attempted by fitting the spectra with Gaussian and Lorentzian models.

Looking at the entire temperature range in figure 4.4, the spectra obtained between 20 and 70 K were well described by a Gaussian lineshape. However, looking at the spectra in figure 4.4 between 400 and 500 mT, a consistent deviation between the high-field parts of the spectra and the fits is observed. Therefore it is apparent that the ferritin-core signals cannot be fully described by a single Gaussian. As the low-field parts of the spectra were well described by these fits, it could be that the correspondence between the ferritin-core signals and the fits is addled by the presence of the six-line signal. Another cause could be that the ferritin-core signal has an asymmetric Gaussian lineshape, rather than the assumed symmetric Gaussian lineshape. This would require the spectra to be fitted using at least two Gaussian models. In either case, it would be useful to define the six-line signal and analyze it simultaneously with the ferritin-core signal, either through simulations or fits. This would improve the analysis of the ferritin-core signal parameters.

The overall lineshape of the ferritin-core signal at 150 K, as shown in figure 4.5, is well described by a Lorentzian lineshape. In the 5 and 10 K spectra no signal resembling the ferritin-core signal is seen. Similar

evolution of the lineshape of the ferritin-core signal was found in ferritin shells loaded with magnetite and/or maghemite [12]. There, however, the ferritin-core signal persisted at 10 K.

On the blocking temperature and A_{pp} Looking at figures 4.2b and 4.3 (in red), the most remarkable observations are the changes in lineshape between 70 and 150 K, and the absence of the ferritin-core signal at 5 and 10 K. Both observations are addressed here through comparison with the model of the magnetic properties of the ferritin core proposed in 1998 by Brooks et al [5].

According to the model proposed by Brooks et al, which is based mainly on magnetometry data and has to this day not been disproven, the ferritin core can be interpreted as being composed of two magnetic layers: an inner and an outer layer, which both have a AFM magnetic order [5]. The inner layer has a Néel temperature above 310 K and antiparallel spins. It can occur, however, that due to the presence of impurities the magnetic sublattices do not fully cancel each other, giving rise to a SPM moment. The SPM moment of the inner layer gives rise to a susceptibility that follows the Langevin law above T_B.

The Fe^{3+} ions composing the outer layer, on the other hand, have a very low Néel temperature, as they experience much weaker exchange forces. This causes the ions in the outer layer to behave like paramagnets. The susceptibility of the outer layer, composed of the disordered surface spins, follows the Curie-Weiss law above the local Néel temperature. The temperature dependence of the susceptibility of these ions is much more gradual than is the case for those following the Langevin law.

Based on the Boltzmann distribution of the spin-population, the lower energy levels of (super)paramagnetic systems - such as the ferritin core above its blocking temperature - become more populated when temperature decreases. Therefore, a Curie-like relation between signal amplitude and temperature, defined as $A_s = CB/T$, is expected. Here, A_s is the signal amplitude, C the material-specific Curie constant and T is the temperature. This Curie-like behaviour is observed for the features described in Section 5.3. The A_{pp} parameter of the ferritin-core signal, however, displays an opposite temperature dependence in the 20-150 K range.

It is very likely that the lineshape changes of the EPR spectra discussed are given by the sum of the SPM component, which follows the Langevin law above T_B, and a Curie-Weiss component, given rise to by the surface spins. The Néel temperature - or perhaps Néel temperature distribution - of the latter is, although unknown, higher than the blocking temperature [5]. It is not known, however, how large the contribution of the Fe^{3+} ions forming the g'=4.3 feature is to this temperature dependence of the susceptibility.

Although there is no universal description of how to determine the blocking temperature from EPR spectra, the blocking temperature of ferritin is here determined based on the reasoning described in [35]. In [35] it was stated for the analysis of AFM/SPM systems, that crossing of T_B affects the line broadening in a way that the signal may no longer, or barely, be detectable.

Based on this, it is expected that the blocking temperature of the ferritin cores lies between 10 and 20 K, as the ferritin-core signal disappears between these two measurements. The signal amplitude of the spectra below 20 K remains above zero, but it is not clear whether this can be an indication of a net magnetization remaining present even at 5 K, or that these are baseline-subtraction artifacts. The signals with the narrow features remaining at 5 and 10 K were described in Section 5.3. The fluctuations present throughout the spectra are ascribed to baseline instabilities.

Considering the temperature dependence of the A_{pp} fit between 20 and 70 K, a positive linear relation was found, as shown in figure 4.6b. Similar behaviour is observed in this temperature range for previously reported spectra [12, 13], where the ferritin shell was loaded with maghemite/magnetite, and for maghemite nanoparticles [26]. The A_{pp} of HoSF EPR spectra also show a similar temperature behaviour, as can be seen in figure B.1. It is also observed in the magnetometry studies of HoSF [20] and ferrihydrite nanoparticles, where the magnetization of the samples decreased with decreasing temperature below the blocking temperature determined under zero-field cooled conditions [33]. Here, analogues can be drawn between magnetometry and EPR data, as the amplitude of the magnetization of the particles influences the signal amplitude in the EPR measurement. A sudden drop measured in the magnetization of a particle using magnetometry would result in a drop in signal amplitude of the corresponding EPR spectra. However, due to the difference in characteristic measurement times, the blocking temperatures cannot be compared without conversion.

The rate of A_{pp} increase between 10 and 30 K might indicate a distribution of blocking temperatures throughout the sample – e.g. due to a distribution of ferritin-core diameters. The gradual decrease of A_{pp}

versus temperature could be due to a distribution of Néel temperatures. Another cause for a T_B distribution could be the presence of minor ferro- and ferrimagnetic phases throughout the core, as proposed by heterogeneous and multiphase models of the iron core (see [2] and references therein).

Although the actual Néel temperature of the ferritin core is at a much higher temperature than T_B, the data does not support the evidence of a magnetic phase transition in the observed temperature range. It can therefore not be said what causes the transition from Lorentzian to Gaussian lineshape observed between 150 and 70 K.

Including the A_{pp} datapoint of 150 K, it can be seen that the relation with temperature will not be linear when including higher temperatures. The relation between A_{pp} and temperature should be determined for a larger temperature range once more spectra have been acquired.

On the resonance field B_{res} One of the models proposed for the temperature dependence analysis of the resonance field B_{res} of magnetic nanoparticles, is described in Section 2.2.2. It predicts that with decreasing temperature the resonance field shifts to lower fields. This predicted behaviour is also observed in the spectra of ferritin molecules loaded with magnetite [13], and in spectra of maghemite nanoparticles [26]. Whether this is also the case for the ferritin spectra acquired in this study is not clear, due to the hindering effect of the six-line signal. Based on the results of the Gaussian model fits the resonance field appears rather stable around 330 mT as the temperature changed. Minor changes in resonance field were also observed in the ferritin molecules loaded with magnetite or maghemite in a similar temperature range studied by [12].

On the resonance broadening ΔB_{pp} Due to the discrepancies of the fits and ferritin-core signals described earlier in this section, the resonance broadening in the 20-70 K range is not clear. However, between 70 and 150 K there is a clear lineshape narrowing as the lineshape changes from partial Gaussian to full Lorentzian. Very small resonance broadening was reported by [12] for ferritin molecules loaded with magnetite or maghemite - which, unlike ferrihydrite, do not have a magnetic transition to AFM order - studied in a similar temperature range.

Evidently, more spectra should be acquired in the range between 70 and 150 K in order to analyze the changes in lineshape better. This was outside the scope of this thesis.

5.5. Discussion of the Easyspin model and the ferritin core composition

To understand the electronic spin structure of the ferritin core, the GSH described in Section 2.2 was used, and rather successfully applied to the 150 K spectrum. This spectrum showed the largest deviations from a Gaussian, was least obscured by the other features, and contained the most structure - a shoulder structure between 50 and 200 mT. It was therefore expected to be the most sensitive to the simulation parameters.

Since ferritin hosts at least 500 Fe^{3+} ions, most of which are magnetically coupled [5, 35], a total spin system of S=10 was considered throughout the simulations and fits of the signal of the magnetic core. This effective spin was used in order to limit computation time and the strain on memory, as proposed in the GSH model introduced in [13]. One should therefore keep in mind that, in order to keep the anisotropy field constant, the in this manner fitted axial ZFS term D is also an effective parameter.

The simulations of the 150 K spectrum using a single spin system and a mainly Lorentzian lineshape could describe the positions of the low- and high-field peaks, but not the shoulder feature between 50 and 200 mT. Neither could it describe the broadening at higher fields. When applied to lower temperatures, the lineshape considered fully Gaussian, the ZFS term became unusable for the interpretation of the temperature dependence. For all temperatures, except for that of the 150 K spectrum, the feature at g'=4.3 could be described well using the simulation parameters described in table 3.1, determined based on this feature in the HoSF spectra.

Using the modeling approach considered in this thesis, a model using a single D parameter, it was not possible to get a complete agreement with the experimental data of the ferritin-core signal.

The best fit was obtained with isotropic g'≈2 (g'=2.0154) - which indicates the presence of magnetite and/or maghemite [12, 24] -, whereas ferrihydrite is typically characterized by isotropic g'=2.1 [2]. This is contradictory to the observation from [23], who attributed the broad EPR signal around g'=2.1 measured in human liver tissue to ferritin cores that exhibit an AFM order at low temperature and SPM with increasing temperature - suggesting therefore the presence of mainly ferrihydrite.

In the HuLiFt spectra a transition from mainly Gaussian to mainly Lorentzian lineshape of the ferritin-core signal is observed with increasing temperature, with a combination being present at the shoulder struc-

ture. This transition suggests that more than one spin system might compose the core. In order to describe the thermal population of the spin states for their spectra, Cini et al. suggested the usage of two weighed and summed spin subsystems of equal effective S and different effective D and $DStrain$ [7]. It is suggested to consider the application of the strategy proposed by Cini et al. [7].

The HSVD-treated spectra and the EELS experiments currently being performed in Oxford by Dr. I. A. M. Ahmed suggest that the core of the studied HuLiFt sample might mainly contain magnetite and/or maghemite, rather than ferrihydrite.

6

Conclusions and Outlook

6.1. Conclusion

In this study a novel approach to analyse 9 GHz EPR spectra, obtained from HuLiFt, is presented. The spectra were background-corrected using a Gaussian derivative fit with linear baseline. Modern signal pre-processing techniques were combined with EPR approaches to extract the ferritin-core signal. This allowed for the preservation of the general lineshape of the ferritin-core signal in an almost completely automated routine. The spectra were analysed using both a phenomenological approach and by employing the Spin Hamiltonian. Although the pre-processing allowed for adequate background corrections and feature extraction for the signal around g'≈2, a six-line signal – most likely caused by manganese impurities – could not be removed, and this interfered with the analysis of the ferritin-core signal.

The phenomenological data analysis showed that in the 20-70 K temperature range the A_{pp} decreases with decreasing temperature, while the lineshape of the ferritin-core signal changes from Lorentzian to Gaussian between 150 and 70 K. The blocking temperature is expected to lie between 10 and 20 K, where the signal amplitude of the ferritin-core signal was lost, indicating a magnetic transition of SPM to ordered AFM magnetization. Whether and how the lineshape shifts or broadens below 70 K cannot be determined due to the six-line signal obscuring the signal in this field range of interest.

In order to study the magnetic properties of the ferritin core, and therefore gain insight on its electronic spin structure, the Spin Hamiltonian was employed. The simplified Giant Spin Hamiltonian model, with a single spin system with total spin $S = 10$, was employed. The spectrum acquired at 150 K was analysed using this approach, since it was the least obscured by other signal components and had a was the most structured - it had a clear shoulder structure at lower fields. as this spectrum contained the most structure and the six-line signal was weakest. The analysis suggests that the ferritin-core signal is centred around g'=2.0154, hinting at a core composition of magnetite or maghemite, rather than of ferrihydrite. Temperature dependent fitting of the ferritin-core signal using Easyspin could not be achieved using the considered model.

6.2. Outlook

In order to improve the understanding of the temperature dependence of the ferritin-core signal and its fitting parameters, it is recommended to acquire spectra in a larger temperature range and to fill the current gap between 70 and 150 K. Furthermore, as the ferritin-core signal appears to be broader than the current field boundaries, it would be meaningful to acquire the spectra in a field range up to 1.5 T.

In order to compensate for the decrease in SNR of the spectra after background correction, as can be seen in figure 3.2a, one might consider to increase the number of scans acquired for each spectrum. Currently each spectrum is composed of eight scans. Therefore, in order to double the SNR, one would need to acquired 32 scans. Due to the instability of the signal baseline over time however, other approaches will have to be explored. Immediately applied could be the option to smooth the buffer spectra while keeping their features and amplitudes intact, prior to subtracting these spectra from the HuLiFt sample spectra. This would lead to a decreased accumulation of noise caused by subtraction.

Concerning the Easyspin parameters, it is recommended to study the crystal structure and size of the ferritin particles (using EELS and HRTEM), and determine the temperature dependent magnetic moment of the sample (using SQUID magnetometry, allowing for the measurement of hystersis curves). For details

on these techniques, see Appendix C. The crystal structure and size measurements would provide insights in the volume distribution of the particles present in the sample and whether the assumption of an uniaxial system is correct. Furthermore, it would allow to determine the lower limit and expected range of blocking temperatures.

Using SQUID magnetometry, the average blocking temperature can be determined. This temperature is different from what would be determined using EPR, but can be converted using equation 3 in Appendix C when knowledge of the remaining parameters is acquired. Hysteresis curves provide insight in the temperature dependence of the saturation magnetization, and therefore of μ and the ground spin state S. Combining this knowledge with the results EELS and HRTEM would provide the anisotropy field – and therefore the true axial ZFS term – can be determined. The effective axial ZFS term can then also be determined, and compared with the EPR results.

Knowledge of these parameters, combined with the extraction of the six-line signal, would improve the Easyspin simulations and fits, and aid in their interpretation.To better approximate the temperature dependence of the lineshape, caused by the temperature dependence of the spin state population, it is recommended to consider the Easyspin fitting approach as suggested in [7] - namely to simulate the ferritin-core signal as the sum of two subsystems, each with identical effective spin, differing only in D and $DStrain$.

To improve fitting accuracy and allow for a better understanding of the temperature dependence of the fitting parameters, it is recommended to further improve the pre-processing procedure. The nature of the six-line signal around g'≈2 and the feature at g'=5.85 should be confirmed, and the temperature dependence of the signals should be identified through Easyspin simulations and fits. The feature at g'=5.85 is thought to belong to methemoglobin. Identification through comparison of its electrophoresis signal - e.g. from the previous SDS PAGE analysis performed to determine the ferritin purity of sample - with that of a reference sample of methemoglobin is recommended.

The six-line signal is thought to belong to manganese impurities. The presence hereof should be confirmed using either inductively coupled plasma mass spectroscopy (ICP-MS), which is a technique that can detect the nature of trace elements and their isotope composition [10], or EELS.

In case of the six-line signal belonging to manganese, it is recommended to use the parameters considered in [4, 15, 31] as initial fitting parameters. If these features are not caused by methemoglobin and manganese, further comparisons with EPR spectra of material found in the human liver should be made.

As previously mentioned, the agreement between experimental data and fits should be improved by identifying and simulating of the six-line signal. This holds for both the phenomenological and the GSH analysis. For the phenomenological fits inclusion of a temperature dependence should be considered in the form of a weight between Gaussian and Lorentzian derivative components.

Bibliography

[1] J. Acosta-Cabronero, M. J. Betts, A. Cardenas-Blanco, S. Yang, and P. J. Nestor. In vivo mri mapping of brain iron deposition across the adult lifespan. *Journal of Neuroscience*, 36(2):364–374, 2016.

[2] I. V. Alenkina, M. I. Oshtrakh, Z. Klencsár, E. Kuzmann, A. V. Chukin, and V. A. Semionkin. 57fe mössbauer spectroscopy and electron paramagnetic resonance studies of human liver ferritin, ferrum lek and maltofer®. *Spectrochimica Acta Part A: Molecular and Biomolecular Spectroscopy*, 130:24–36, 2014.

[3] C. M. Barnés, E. C. Theil, and K. N. Raymond. Iron uptake in ferritin is blocked by binding of [cr(tren)(h2o)(oh)]2+, a slow dissociating model for [fe(h2o)6]2+. *Proceedings of the National Academy of Sciences*, 99(8):5195–5200, 2002. ISSN 0027-8424. doi: 10.1073/pnas.032089399. URL `https://www.pnas.org/content/99/8/5195`.

[4] S. Blanchard, G. Blain, E. Rivière, M. Nierlich, and G. Blondin. Temperature dependence of x-and q-band epr spectra of the dinuclear manganese(ii) complex $[(no_2bpmp)\ mn_2\ (\mu\text{-}oac)_2]^+$: Determination of the exchange constant and of the spin parameters for the s= 1, 2, and 3 spin states. *Chemistry–A European Journal*, 9(17):4260–4268, 2003.

[5] R. A. Brooks, J. Vymazal, R. B. Goldfarb, J. W. Bulte, and P. Aisen. Relaxometry and magnetometry of ferritin. *Magn Reson Med*, 40(2):227–235, Aug 1998.

[6] M. Bulk, L. van der Weerd, W. Breimer, N. Lebedev, A. Webb, J. J. Goeman, R. J. Ward, M. Huber, T. H. Oosterkamp, and L. Bossoni. Quantitative comparison of different iron forms in the temporal cortex of alzheimer patients and control subjects. *Scientific reports*, 8(1):1–11, 2018.

[7] A. Cini, P. Ceci, E. Falvo, D. Gatteschi, and M. Fittipaldi. An epr study of small magnetic nanoparticles. *ZEITSCHRIFT FUR PHYSIKALISCHE CHEMIE-INTERNATIONAL JOURNAL OF RESEARCH IN PHYSICAL CHEMISTRY & CHEMICAL PHYSICS*, 231(4, SI):745–757, APR 2017. ISSN 0942-9352. doi: 10.1515/zpch-2016-0846.

[8] James R Connor, Brian S Snyder, Paolo Arosio, David A Loeffler, and Peter LeWitt. A quantitative analysis of isoferritins in select regions of aged, parkinsonian, and alzheimer's diseased brains. *Journal of neurochemistry*, 65(2):717–724, 1995.

[9] J. Emsley. *Nature's Building Blocks: An A-Z Guide to the Elements*. Oxford Pakistan Paperbacks Series. Oxford University Press, 2001. ISBN 9780198503415. URL `https://books.google.nl/books?id=Yhi5X7OwuGkC`.

[10] TU Delft Faculteit Civiele Techniek en Geowetenschappen. Inductively coupled plasma mass spectrometry (icp-ms). `https://www.tudelft.nl/citg/over-faculteit/afdelingen/watermanagement/research/waterlab/equipment/inductively-coupled-plasma-mass-spectrometry-icp-ms/`. Last accessed: 23-10-2020.

[11] M. Fittipaldi, L. Sorace, A-L Barra, C. Sangregorio, R. Sessoli, and D. Gatteschi. Molecular nanomagnets and magnetic nanoparticles: The emr contribution to a common approach. *Physical chemistry chemical physics : PCCP*, 11:6555–68, 09 2009. doi: 10.1039/b905880j.

[12] M. Fittipaldi, C. Innocenti, P. Ceci, C. Sangregorio, L. Castelli, L. Sorace, and D. Gatteschi. Looking for quantum effects in magnetic nanoparticles using the molecular nanomagnet approach. *Phys. Rev. B*, 83, 03 2011. doi: 10.1103/PhysRevB.83.104409.

[13] M. Fittipaldi, R. Mercatelli, S. Sottini, P. Ceci, E. Falvo, and D. Gatteschi. Sensing the quantum behaviour of magnetic nanoparticles by electron magnetic resonance. *Physical chemistry chemical physics : PCCP*, 18, 01 2016. doi: 10.1039/c5cp07018j.

[14] D. Gatteschi, R. Sessoli, and J. Villain. *Molecular Nanomagnets*. Oxford University Press, Oxford, UK, 2006. ISBN 9780198567530.

[15] A. P. Golombek and M. P. Hendrich. Quantitative analysis of dinuclear manganese (ii) epr spectra. *Journal of Magnetic Resonance*, 165(1):33–48, 2003.

[16] Tjisse Hiemstra. Surface structure controlling nanoparticle behavior: magnetism of ferrihydrite, magnetite, and maghemite. *Environmental Science: Nano*, 5(3):752–764, 2018.

[17] S. M. Kay and S. L. Marple. Spectrum analysis—a modern perspective. *Proceedings of the IEEE*, 69(11): 1380–1419, 1981.

[18] K. Komosinska-Vassev, P. Olczyk, J. Kasperczyk, B. Pilawa, R. Krzyminiewski, B. Dobosz, P. Ramos, J. Stojko, M. Stojko, D. Ivanova, et al. Epr spectroscopic examination of different types of paramagnetic centers in the blood in the course of burn healing. *Oxidative Medicine and Cellular Longevity*, 2019, 2019.

[19] T. Kubiak, R. Krzyminiewski, and B. Dobosz. Epr study of paramagnetic centers in human blood. *Current Topics in Biophysics*, 36(1):7–13, 2013.

[20] P. Kumar, M. Bulk, A. Webb, L. van der Weerd, T. Oosterkamp, M. Huber, and L. Bossoni. A novel approach to quantify different iron forms in ex-vivo human brain tissue. *Scientific Reports*, 6:38916, 12 2016. doi: 10.1038/srep38916.

[21] R. Maurice, C. de Graaf, and N. Guihéry. Magnetic anisotropy in binuclear complexes in the weak-exchange limit: From the multispin to the giant-spin hamiltonian. *Phys. Rev. B*, 81:214427, Jun 2010. doi: 10.1103/PhysRevB.81.214427. URL `https://link.aps.org/doi/10.1103/PhysRevB.81.214427`.

[22] C. A. May, J. K. Grady, T. M. Laue, M. Poli, P. Arosio, and N. D. Chasteen. The sedimentation properties of ferritins. New insights and analysis of methods of nanoparticle preparation. *Biochim. Biophys. Acta*, 1800(8):858–870, Aug 2010.

[23] E. Mosiniewicz-Szablewska, A. Slawska-Waniewska, K. Swiatek, N. Nedelko, J. Galazka-Friedman, and A. Friedman. Electron paramagnetic resonance studies of human liver tissues. *APPLIED MAGNETIC RESONANCE*, 24(3-4):429–435, 2003. ISSN 0937-9347. doi: 10.1007/BF03166946. 31st Congress of AMPERE, POZNAN, POLAND, 2002.

[24] V. Nandwana, S. R. Ryoo, S. Kanthala, A. Kumar, A. Sharma, F. C. Castro, Y. Li, B. Hoffman, S. Lim, and V. P. Dravid. Engineered ferritin nanocages as natural contrast agents in magnetic resonance imaging. *RSC ADVANCES*, 7(55):34892–34900, 2017. ISSN 2046-2069. doi: 10.1039/c7ra05681h.

[25] S. Narayanan, R. Shahbazian-Yassar, and T. Shokuhfar. Transmission electron microscopy of the iron oxide core in ferritin proteins: current status and future directions. *Journal of Physics D: Applied Physics*, 52(45):453001, 2019.

[26] N. Noginova, F. Chen, T. Weaver, E. P. Giannelis, A. B. Bourlinos, and V. A. Atsarkin. Magnetic resonance in nanoparticles: between ferro-and paramagnetism. *Journal of Physics: Condensed Matter*, 19(24):246208, 2007.

[27] R. A. F. Penrose. The chemical relation of iron and manganese in sedimentary rocks. *The Journal of Geology*, 1(4):356–370, 1893. ISSN 00221376, 15375269. URL `http://www.jstor.org/stable/30054302`.

[28] C. Quintana and L. Gutiérrez. Could a dysfunction of ferritin be a determinant factor in the aetiology of some neurodegenerative diseases? *Biochimica et Biophysica Acta (BBA)-General Subjects*, 1800(8): 770–782, 2010.

[29] C. Quintana, J. M. Cowley, and C. Marhic. Electron nanodiffraction and high-resolution electron microscopy studies of the structure and composition of physiological and pathological ferritin. *Journal of structural biology*, 147(2):166–178, 2004.

[30] D. E. Schwab, J. S. Stamler, and D. J. Singel. Epr spectroscopy of nitrite complexes of methemoglobin. *Inorganic chemistry*, 49(14):6330–6337, 2010.

[31] R. Silva, P. Morais, F. Qu, A. Alcalde, N. Dantas, and H. Sullasi. Synthesis process controlled magnetic properties of pb1xmnxs nanocrystals. *Applied Physics Letters*, 90:253114–253114, 06 2007. doi: 10.1063/1.2746076.

[32] S. Stoll and A. Schweiger. Easyspin, a comprehensive software package for spectral simulation and analysis in epr. *Journal of Magnetic Resonance*, 178(1):42 – 55, 2006. ISSN 1090-7807. doi: https://doi.org/10.1016/j.jmr.2005.08.013. URL `http://www.sciencedirect.com/science/article/pii/S1090780705002892`.

[33] S. V. Stolyar, D. A. Balaev, V. P. Ladygina, A. I. Pankrats, R. N. Yaroslavtsev, D. A. Velikanov, and R. S. Iskhakov. Ferromagnetic resonance study of biogenic ferrihydrite nanoparticles: Spin-glass state of surface spins. *JETP Letters*, 111:183–187, 2020.

[34] L Vanhamme, R. D. Fierro, S Van Huffel, and R de Beer. Fast removal of residual water in proton spectra. *JOURNAL OF MAGNETIC RESONANCE*, 132(2):197–203, JUN 1998. ISSN 1090-7807. doi: 10.1006/jmre.1998.1425.

[35] M. P. Weir, T. J. Peters, and J. F. Gibson. Electron spin resonance studies of splenic ferritin and haemosiderin. *Biochimica et biophysica acta*, 828(3):298–305, 1985. ISSN 0006-3002. doi: 10.1016/0167-4838(85)90311-5.

[36] S. A. You and Q. Wang. Ferritin in atherosclerosis. *Clinica Chimica Acta*, 357(1):1–16, 2005.

Appendices

A. EPR experimental protocol: used for spectrum acquisition of HuLiFt and buffer

At the start of each measurement week, a liquid helium vessel was connected to the EPR cryostat through a helium transfer line, in order to allow measurement at cryogenic temperatures. Throughout the measurements, the helium vessel was connected with the helium reservoir of the facility through a recovery line, in which helium flow was allowed when no measurements were being performed.

Each measurement day was started by warming up the electronics for one hour, and simultaneously lowering the temperature in the cryostat by fully opening the needle valve of the helium transfer line, after an overpressure of 0.5 bar was manually created inside the vessel. The overpressure was created at the start of the measurement day, and released by the end of it.

Once the temperature of the cryostat, as registered by a three-term controller, had reached 75±5 K, the sample - before that point stored and immersed in nitrogen - was placed inside the dewar located in the cavity. As the temperature of the system further decreased to 3 K, the target temperature specific parameters for the three-term controller were set. The three-term controller is a control loop that brings the measured temperature to the set temperature based on the provided proportional (P), integral (I), derivative (D) terms provided with the set temperature. The PID values for each set temperature used are given in table A.1.

Once the temperature of the system reached 3 K, the needle valve was fully closed, causing the temperature of the system to increase. Upon reaching a temperature of about 10 K higher than the target temperature, the needle valve was opened in small increments, resulting in a slow decrease of the rate of temperature increase, and later a decrease of the temperature. Reaching a slowly decreasing temperature of approximately 20 K below the target temperature, the heater settings of the three-term controller were changed from manual to automatic, inducing the start of the feedback loop.

Starting at the point the temperature increases during automatic heating, the temperature in the system, the number of heater bars, and the amount of overpressure in the helium vessel were noted every ten minutes, for three to four iterations. After this time, the fluctuations in temperature tended to be minor, and the measurement was performed after an additional 30 minutes of temperature stabilization. In the case of measurement at 5 K, or temperatures equal or higher than 100 K, this final stabilization took one hour.

While waiting for the final temperature stabilization, the measurement program (Xepr, Bruker) was prepared, and the settings for measurement were set, in this case, to 2.946 mT of modulation amplitude, 10 dB of attenuation (i.e. 20 mW), 90 kHz modulation frequency. EPR measurements performed were continuous-wave (CW) measurements (for more information, see section 3.2 in Appendix C), in a 9 GHz ELEXSYS E680 EPR spectrometer (Bruker), equipped with a rectangular cavity (ER 4102ST). Each measurement was the average of eight scans, acquired on a field range of 50-850 mT. Depending on the signal-to-noise ratio, a different number of scans might be required. Accumulation time of a spectrum consisting of eight scans required a scan time of 11.2 minutes.

Scans were aborted if the slope of the measurement fluctuated strongly between scans. Since temperature instabilities may cause such fluctuations, if that occurred, the temperature was left to stabilize for an additional ten minutes before repeating the fine-tuning and stabilizing the system parameters - the diode current and the lock offset - and remeasuring the sample at that temperature.

Temperature changes between measurements were made after setting the magnetic field to zero, to achieve zero-field cooled acquisition. Corresponding PID values were defined in the three-term controller, and the procedure was repeated by closing the needle valve and letting the temperature increase to 10K above the target temperature, and repeating the steps described above.

At the start of each measurement day, the final measurement of the previous day was repeated to check for reproducibility.

Table A.1: Temperature specific PID values as used for the stabilization of the temperatures used in the CW-EPR X-band measurements performed during this study. For stabilization at temperatures between 80 and 150 K, the PID values as provided for 150 K are advised.

Temperature [K]	**P**	**I**	**D**
5	30	1	0
10	35	1	0
20	35	1	0
30	30	1.5	0.2
40	30	1.5	0.2
50	28	1.8	0.3
60	23	2	0.3
70	23	2	0.3
150	15	2.5	0.5

B. Description of temperature dependent 9 GHz EPR spectra of horse spleen ferritin

Temperature dependent EPR spectra of ferritin, mainly studied in the form isolated from horse spleen (HoSF), are shown in figure B.1. These spectra were acquired during a previous study of HoSF [20] and were baseline-corrected using the method described in Section 3.3.1-HoSF. The general structure of the ferritin signal can well be observed in the 231 K spectrum in figure B.1a.

The spectrum has a broad feature around g'=2.1 with a peak-to-peak linewidth - called resonance broadening ΔB_{pp} - of ~220 mT. This broad feature is caused by a system with a large S [11], and is henceforth referred to as the ferritin-core signal. The core of HoSF is composed of ferrihydrite [2, 23, 35]. Other features present are narrow and located around g'=4.3 and g'=2. The feature at g'=4.3 is assigned to aspecific rhombic Fe^{3+} sites [20], while the narrow feature at g'=2 is caused by radicals.

As can be seen when comparing the baseline-corrected spectra in figure B.1, reconstructed from the data provided by [20], the signal amplitudes of the features at g'=4.3 and g'=2 increase with decreasing temperature, and do not shift in resonance field B_{res}.

In figure B.1b the spectra from figure B.1a are overlayed and zoomed-in. As can be seen, the intensity of the ferritin-core signal around g'=2.1 decreases with decreasing temperature, while the spread increases. Observing the spectra acquired at 50 and 20 K, there is an abrupt change in lineshape, where the ferritin-core signal disappears. This change is due to the crossing of the blocking temperature, corresponding with a magnetic phase transition which is possibly of antiferromagnetic nature and renders no signal intensity when measured with EPR.

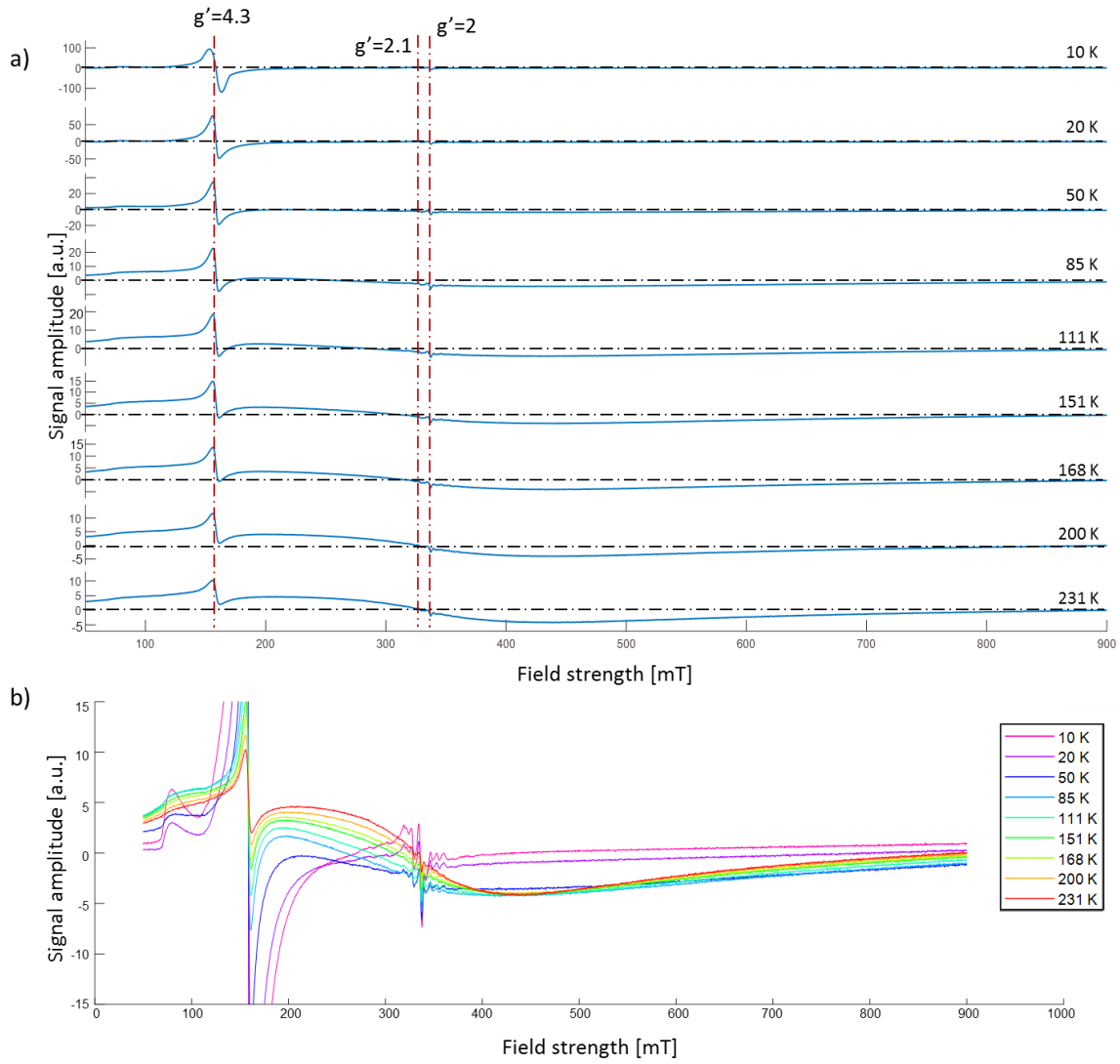

Figure B.1: Baseline-corrected EPR spectra of HoSF. Raw data acquired at different temperatures at 9 GHz [20]: 6 G modulation amplitude, 15 dB attenuation, 9.49 GHz microwave frequency. Acquired in a field range of 50-950 mT. In case of premature intensity clipping of peaks, a spline interpolation was performed on the data, in order to restore the expected signal shape, such that simulations and fits of its features could properly be performed. a) Main features indicated are: g'=2.1 (broad signal: mineral core of ferritin); around g'=4.3 (aspecific rhombic Fe^{3+} sites); around g'=2 (narrow signal: radical). b) Zoom-in of all overlayed spectra is presented, showing the evolution of the lineshape of the ferritin core signal under the influence of measurement temperature.

C. Literature review: Overview of magnetic properties of ferritin nanoparticles

Overview of magnetic properties of ferritin nanoparticles

Vera Čaluković

Abstract

Ferritin is one of the main iron regulation proteins in the body, and has been studied extensively over the past 70 years. This literature study aims to provide a clear overview of: (i) the magnetic properties of the minerals stored inside the ferritin core; (ii) the current state-of-the-art techniques used in the study of iron-oxide nanoparticles (i.e. nuclear magnetic resonance techniques, electron paramagnetic resonance, Mössbauer spectroscopy, magnetometry, high-resolution transmission electron microscopy and electron energy loss spectroscopy); (iii) present day knowledge of ferritin.
As each of the techniques used in the study of this complex protein has different sensitivities, we foresee that new insights on the magnetic properties of ferritin can be gained through complementation of multiple techniques.

Table of content

1. Introduction

Ferritin is the main iron storage protein in mammalians and plants. As such, its main function is that of iron ion homeostasis on a systemic level and in the brain [1], [2]. The study of ferritin therefore plays a large role in the study of both haemoglobinopathies, such as atherosclerosis [3] and anaemia, and (motor) neurodegenerative diseases, such as Alzheimer's disease (AD), Parkinson's disease (PD) and progressive supranuclear palsy (PSP) [4].

The molecular properties, structure and function of ferritin have been extensively studied since the 1950s. Ferritin has been established to be a spherical protein with full diameter of 12 nm, consisting of an organic shell and inorganic core.

The organic shell of ferritin in humans consists of 24 protein subunits, each of which can be either a heavy (H; molar weight $21x10^3$ u) or light (L; molar weight $19x10^3$ u) subunit [4]. The ratio of subunits present in the shell depends on the organ the ferritin is considered in, and it is directly related to the predominant function played by the protein.
For example, a relatively high H/L ratio, as found in the heart and the brain, leads to a focus on iron oxidation: free ferrous iron (Fe^{2+}) is bound in the binding sites present in H subunits and converted into ferric iron (Fe^{3+}) – a less toxic and reactive form of iron [5]. The process through which oxidation takes place has been extensively studied, and is explained in a clear manner in [6]. For humans there is known to be variation in H/L ratios within different regions of the brain and between different cells [4].
In organs that contain large amounts of iron, such as the liver and spleen, a relatively low H/L ratio is observed. This ratio indicates the need for a large iron storage capacity, which is provided for by the high density of L subunits [5]. This decrease in shell thickness leads to an increase in the ferritin core size and mineralized iron storage capacity. In these ferritin proteins iron oxidation still takes place, merely the emphasis is shifted to mineralization and storage. It has been suggested that the presence of L subunits enhances the activity of H subunits, leading to a larger number of fully oxidized iron ions stored into the cavity [7].

Once Fe^{2+} iron has been converted to Fe^{3+} iron, it slowly mineralizes inside the ferritin core in the form of, among others, ferrihydrite, magnetite and/or maghemite and hematite. The diameter of the ferritin core is dependent on the shell composition and the amount of iron stored inside it, and generally ranges between 5 and 8 nm. The core is thought to have a maximum capacity of 4500 iron atoms *in vitro*, and average loading *in vivo* is generally reported to be between 1000 and 1500 iron atoms (see refs 70, 71 in [8]). When the core is devoid of iron, ferritin is referred to as apoferritin. Apoferritin is often synthetically manipulated in order to create proteins such as magnetoferritin, a protein used in several biomedical applications, presenting an apoferritin shell and a magnetite or maghemite core – for a recent overview on magnetoferritin, see [9]. In this study, the relevant iron-(hydr-)oxides will be:

Ferrihydrite – Ferrihydrite is an iron hydroxide mineral of which the spin structure is highly debated, and which is inside ferritin generally characterized by antiferromagnetic ordering. It is defined by the formula $Fe_2O_3*0.5H_2O$, and the iron ions it consists of are solely Fe^{3+}. Coordination of ligands around each iron ion are either tetrahedral or octahedral, as shown in figure 1, and evidence suggests that ferrihydrite crystals consist of a mix of the two [10], [11] – a model proposed by Michel et al (see refs 24, 25 in [11]). Chemical stability analysis of a large ferrihydrite particle size distribution – using surface depletion models that describe theoretical ferrimagnetic and antiferromagnetic ferrihydrite cores – suggest that ferrimagnetic core ordering is chemically more stable than antiferromagnetic ordering for diameters smaller than ~4 nm [10].

Hematite - Hematite is defined by the formula α-Fe_2O_3, and is the dehydrated and aged form of ferrihydrite [10].

Magnetite - Magnetite is defined by the formula Fe_3O_4, and contains both Fe^{3+} and Fe^{2+} [10]. Its crystal structure consists of both a tetrahedral and an octahedral coordination, where half of the Fe^{3+} is in the tetrahedral coordination and all Fe^{2+} and half the Fe^{3+} make up the octahedral coordination. The orientation of the octahedral and tetrahedral Fe^{3+} magnetic moments is opposite, and thus the total magnetic moment of the crystal arises from the uncompensated octahedral Fe^{2+} ions [12].

Maghemite - The oxidation product of magnetite, is defined by the formula γ-Fe_2O_3, and contains only Fe^{3+} [10]. Similarly to magnetite, maghemite's crystal structure also consists of both a tetrahedral (62.5% of the Fe^{3+} ions) and an octahedral (37.5% of the Fe^{3+} ions) coordination. Both magnetite and maghemite behave ferrimagnetically at room temperature.

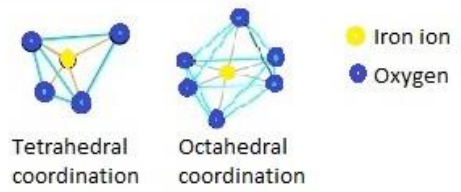

Figure 1: Schematic representation of tetrahedral and octahedral coordination of a central iron ion, either Fe^{2+}or Fe^{3+}, with oxygen atoms. In tetrahedral coordination four oxygen atoms are arranged around the iron ion, while in octahedral coordination six oxygen atoms are arranged around the iron ion.

In 1998 a model for the magnetic properties of ferritin was proposed by Brooks et al [13]. This model describes the core as consisting of an inner core and an outer layer, as illustrated in figure 2. While the inner core is magnetically ordered with antiferromagnetic and superparamagnetic properties – due to crystal defects – the outer layer is antiferromagnetic and magnetically disordered. The inner core has, due to its ordering, a higher Néel temperature than the disordered layer.

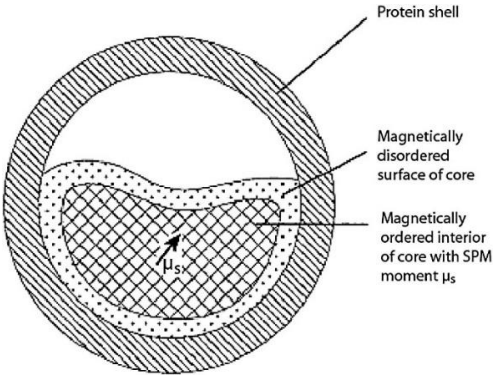

Figure 2: Model of the magnetic properties of ferritin as proposed by Brooks et al. Ferritin core consists of a magnetically ordered inner core (cross-hatched), either solely antiferromagnetic, or both antiferromagnetic and superparamagnetic (magnetic moment of superparamagnetic fraction indicated with the arrow), and a magnetically disordered outer layer (dotted). The protein shell is indicated with linear hatches. ***No permission for reproduction asked.***

The above model exemplifies the complexity of the magnetic properties of ferritin, and shows why, after many years, this protein is still a subject of scientific interest for the condensed matter community.

Final version literature study: Overview of magnetic properties of ferritin nanoparticles
Vera Čaluković, 4713419
2020

The current literature study aims to summarize and discuss the magnetic properties of ferritin, as studied by magnetic analyses, magnetic resonance techniques and high resolution (HR) transmission electron microscopy (TEM) to date.

In Section 3 a general overview on magnetic order and techniques used to measure the magnetic properties of ferritin is presented. The results and insights acquired through measurement of these properties are discussed in Section 4. The design of the literature study is discussed in Section 2.

2. Literature study design

The database used for this study was Web of Science, as it has the advantage of a broad research reach, collects peer reviewed and high quality articles, features a clear Boolean search approach and good recall and reproducibility performance; aspects that are needed for a database to be the primary database in a systematic review [14]. PubMed was not used, due to the emphasis of the search on physical properties, rather than medical studies, and certain journals – such as Physics Review B – were not included in the PubMed database. Most queries were conducted from the same IP address, and all searches were conducted at the Leiden University institution. Extent of search results may therefore vary when conducted through another institution using the same queries as used during this study.

Literature was gathered by considering the combined results acquired from the three search queries described in table 1.

As the initial search provided a large number of papers, of which many were not specific to the topics at hand, the second query was set up – with additional search terms based on knowledge acquired from several papers of the first query. The results from the second query were extracted after refinement and analysed using the literature categorization program VOSviewer [15], which allowed for the creation of the term connection map as shown in figure 3. Looking at the articles presented in the results and zooming in on the terms connected to "ferritin core", lead to the conclusion that specification of "superparamanet*" was a good addition to the search query, as several terms were specific to the research topic at hand. Through specification of the main minerals present inside ferritin, all known to behave superparamagnetically, the final search query was created.

Relevance of articles obtained was initially judged on basis of title and abstract, and later also on conclusion, figures and introduction. An article was deemed relevant if it focussed on the study of one or more magnetic properties of (minerals inside) the ferritin core, the methodology was explained appropriately, it contained enough focus on the physics and it was not too specifically focussed on applications.

Table 1: Overview of used search queries within Web of Science. Refinement options used, the number of entries each search resulted in, and the date the search was last performed on are mentioned. Furthermore, in case VOSviewer was used, the threshold values used are also mentioned. (n = number of times a term was used throughout all titles and abstracts considered; % = the percentage of most relevant terms found within the database after initial threshold n). Relevance of terms was calculated inside VOSviewer, the user had no influence on the method this calculation was performed.

Search query	Refinement	#Results	Date	VOSviewer
"ferritin$ AND magneti* AND propert*" [TOPIC]	-	323	10-01-2019	-
"ferritin$ OR magnetoferritin" [TITLE] AND "superparamagnet*" [TOPIC]	Journals included: physical condensed matter OR biophysics OR spectroscopy OR physics atomic molecular chemical OR multidisciplinary sciences OR physics applied Timespan included: 1980-2020	868	16-02-2020	Binary counting; n= 10; % = 60)
"(ferritin$ AND ferrihydrite) OR (ferritin$ AND magnetite) OR magnetoferritin" [ALL FIELDS] AND "superparamagnet*" [TOPIC]	Timespan included: 1968-2020	82	16-02-2020	-

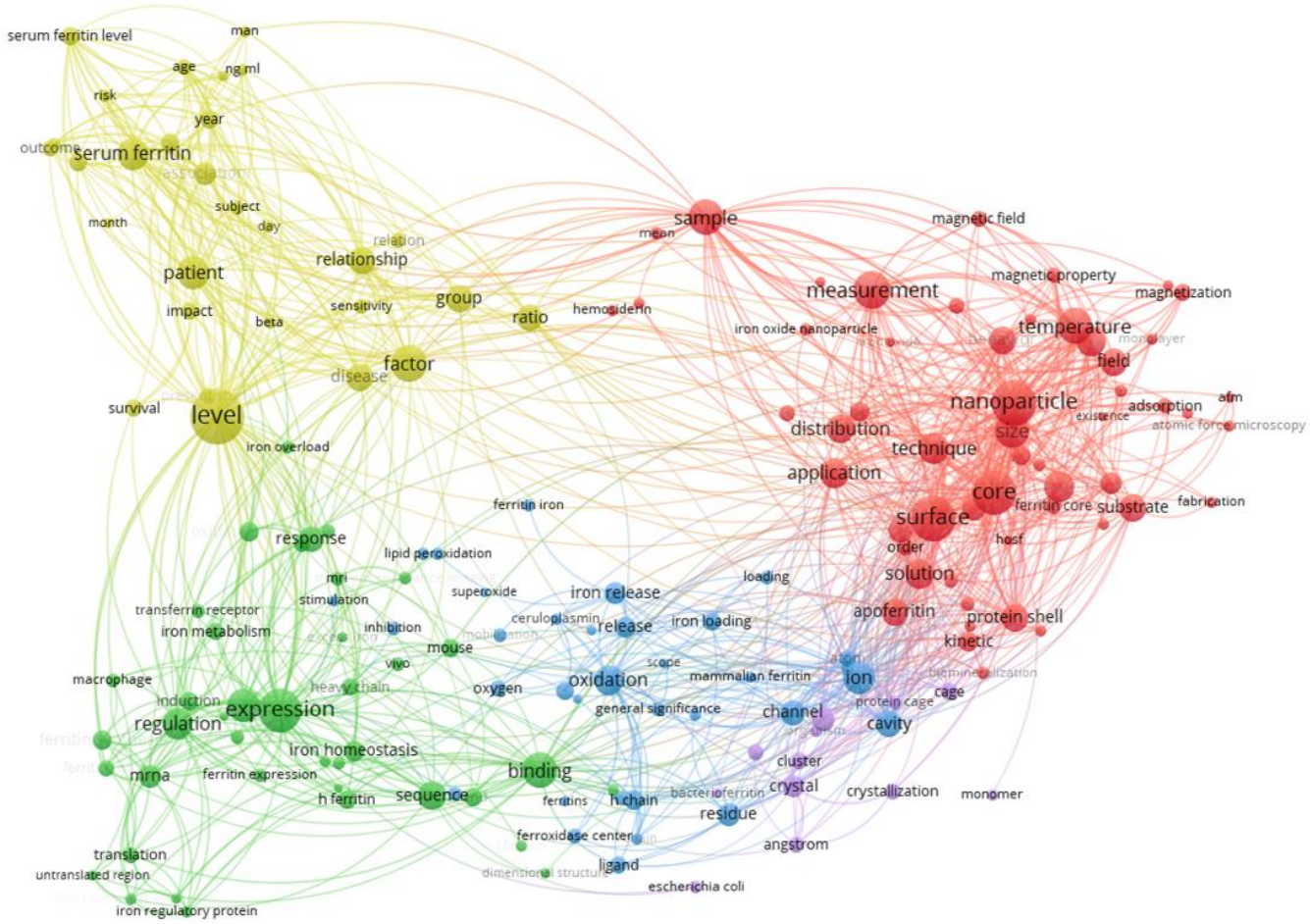

Figure 3: Term map made with VOSviewer, based on the terms used in the articles acquired with the second search query described in table 1. The different colours represent the different clusters to which terms belong. The relative size of the spheres corresponds to the occurance of the respective terms. Terms that are regularly used together within title and abstract are shown connected.

3. Magnetic properties, techniques used to measure them, and EELS

3.1 Types of magnetic orders

Different iron-oxides can have different magnetic properties, which can be determined under the effect of magnetic fields and changes in temperature. Through determination of the magnetic susceptibility χ of a material or molecule, it is possible to differentiate between different types of magnetic ordering [16]. The static magnetic susceptibility as a function of temperature can, for example, be studied using magnetometry, as $\chi = dM/dB$. Here, M is the magnetization of the material – the density of magnetic dipole moments inside a magnetic material – and B the externally applied magnetic field.

Four types of magnetic order are relevant to this study:

Ferromagnetism - Above its Curie temperature, a ferromagnetic material behaves like a paramagnet - in the absence of an externally applied magnetic field B it has null net magnetic moment due to its disordered magnetic moments; in the presence of B the magnetic moments align parallel to the field

and the material has a non-null net magnetic moment. Below its Curie temperature, the magnetic moments are aligned parallel to each other despite the absence of B, and the material therefore has non-null net magnetic moment.

Ferrimagnetism - Similarly to ferromagnetic materials, ferrimagnetic materials behave paramagnetic above their Curie temperature, and have, in the absence of B, a non-null net magnetic moment at temperatures below their Curie temperature. Contrary to ferromagnetic materials, however, the magnetic moments of ferrimagnetic materials are aligned antiparallel to each other. The lattice in which the magnetic moments are present can be interpreted as consisting of two sublattices. The magnetic moments in these sublattices are opposite in orientation, but not equal in magnitude, resulting in a non-null magnetic moment.

Antiferromagnetism - For antiferromagnetic materials not the Curie temperature, but rather the Néel temperature, is used in the distinction between the two magnetic behaviours. Above the Néel temperature the material behaves as a paramagnetic material, while below the Néel temperature the magnetic moments align antiparallel to each other. Contrary to the magnetic behaviour detected in ferrimagnets however, the magnetic moments in the sublattices of an antiferromagnetic material are both opposite in orientation and equal in magnitude. Because of this, a net null magnetization is found.

Superparamagenetism - Superparamagnetism is a property observed in particles, such as the minerals present in the ferritin core, of nanometre size [17]. Due to the magnetic moments of these minerals, and the size of its core, ferritin nanoparticles are composed of a single magnetic domain. Furthermore, paramagnetic behaviour is observed in these nanoparticles even below the Curie and Néel temperatures. Instead of being stable in the absence of a magnetic field, however, the magnetic moment orientation of the nanoparticles fluctuates between two stable anisotropy energy states, ε, separated by an energy barrier E [18]. The energy barrier is equal to the magnetic anisotropy of the particle, K, multiplied with its volume V, while $\varepsilon = KV\sin^2(\theta)$. θ is the angle between the magnetization vector and the uniaxial magnetic anisotropy axis (i.e. the axis along which the fluctuations occur). As the temperature is further decreased the Néel relaxation time (τ_N), the time between two spin flips, increases. The relation between τ_N and temperature T is given by:

$$\tau_N = \tau_0 \exp(E/k_BT) . \quad (1)$$

τ_0 is the characteristic relaxation time – ranges between 10^{-9} and 10^{-13} s (see ref 20 in [18]), although more often observed between 10^{-11} and 10^{-13} s [18] – and k_B is the Boltzmann constant.

3.2 State-of-the-art techniques for iron-oxide nanoparticle studies

Measurement techniques that are often used in the analysis of magnetic properties of ferritin can be roughly divided into three categories: (i) magnetic resonance-based techniques, (ii) techniques that measure magnetic properties through magnetic flux induction, and without on-resonance effects and (iii) techniques that measure energy loss of transmitted electrons after elastic and inelastic scattering. Several techniques falling under these categories are briefly discussed below. In table 2 technique corresponding measurement frequency (n) range, measured properties and magnetic field strength (B) are summarized. Apart from MRI, which operates mainly at ~300 K only, the other listed techniques can operate additionally at cryogenic temperatures.

3.2.1 Magnetic resonance-based

Magnetic resonance based techniques are used for measurements of systems with a total non-zero nuclear/electron spin. Nuclear magnetic resonance based techniques, such as nuclear magnetic resonance (NMR) and magnetic resonance imaging (MRI), are used for the study of systems with nuclei of $I \neq 0$, while electron paramagnetic resonance (EPR) techniques are used in the study of systems with unpaired electrons and μSR [19] targets polarized muon spins interacting with a sample.

The particles (protons, electrons, muons, etc.; denoted with subscript *x*) within a sample precess with a frequency called the Larmor frequency n_L, which is particle-specific and defined as $n_L = \gamma_x B_0$ when placed in an external magnetic field B_0 [20]. The gyromagnetic ratio, γ_x, is defined as $\gamma_x = g_x \mu_x / \hbar$, where $\hbar$ is the Planck constant, μ_x is the magnetic moment of particle *x*, and g_x is the Landé *g*-factor specific to the electrons.

In the specific case of EPR, the g-factor of the free electron, g = 2.00231, is influenced by the molecule (radical) or metal ion it is associated with. The resulting g-tensor contains information about this environment.

For all the above-mentioned techniques (with the exception of μSR), energy of an oscillating magnetic field B_1 – perpendicular to B_0, and with frequency equal to the Larmor frequency – is absorbed by the system upon irradiation, and is measured as the change in energy.

In the case of NMR, the magnetic moment μ_x is that of the nucleus of the isotope inspected (μ_N), and resonance occurs at isotope specific frequencies [20]. The signal is formed when the time-varying magnetization, after an initial perturbation has taken place, induces an electromotive force in the induction coil [16]. The global setup for NMR is depicted in figure 4(a).

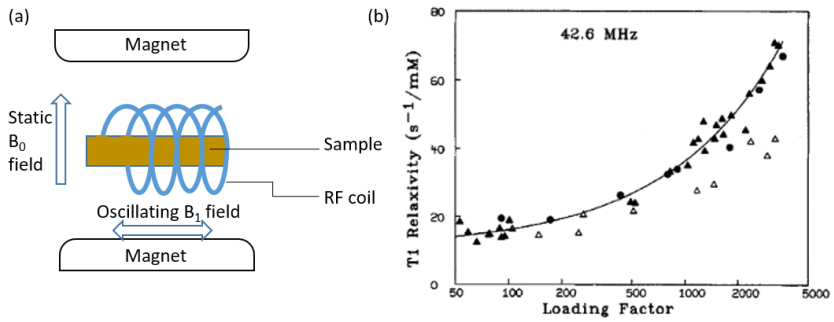

Figure 4: Schematic representation of NMR and MRI T_1 relaxivity (b) acquired therewith. The setup consists of a sample placed inside a static B_0 field generated by opposing magnets. A radiofrequency (RF) coil is placed around the sample, and picks up the signal generated through the effect of an oscillating B_1 field working on the nuclear spins present within the sample. Using this setup, measurements of the T_1 relaxivity (r_1) can be performed, for example, on apoferritin under the influence of increasing iron concentration inside the ferritin core (b). Data (triangles; open have been discarded in the fitting) was acquired by Brooks et al. 1998 [13]. ***No permission for reproduction asked.***

Magnetic resonance imaging follows the same principles as NMR and the setup is similar, although different protocols are used as it is used in healthcare mainly. The signal is generally acquired from protons, although detection of other nuclei is also possible. In the study of ferritin the focus is laid on relaxometry measurements, i.e. the effect ferritin has on the relaxation rates of protons.

Relaxometry is the study of the recovery/decay of the longitudinal/transverse magnetization, upon lifting of a perturbation. These relaxation times are named T_1 and T_2 respectively. The relaxation rates

(R_i) – with i = 1, 2 – is the inverse of these relaxation times. Additionally, relaxivity (r_i) is defined as the ratio $r_i=R_i/$[molecule or ion].

It was shown by Brooks et al. that the r_1 and r_2 of ferritin depend on the loading factor (LF), i.e. the amount of iron ions loaded into its core, and the temperature and field strength at which measurements are performed at [13]. In figure 4(b) the relation between r_1 and LF is plotted [13].

When the magnetic moments of unpaired electrons are of interest, EPR is used. Here, the magnetic moment μ_x equals the Bohr magneton μ_B.

The EPR spectrum is measured through detection of microwave power reflected at the cavity when a microwave absorption event occurs [20]. The g-factor at which this signal occurs is used to infer the magnetic and angular moments of the unpaired electrons, and their interactions with nearby electron and nuclear spins. In this manner, by determination of both the presence and strength of unpaired electrons, specific elements – when their spectra are known – and the relative concentrations thereof within a sample are determined. The signal is detected as the first derivative of the absorption. An example of an EPR signal of HoSF, measured at different temperatures, is shown in figure 5(b) [21]. Field strength of B_0 is given in Gauss (1T = 10^4 G). The difference between the signal detection methods of NMR/MRI and EPR is due to the setup, which for EPR is shown schematically in figure 5(a).

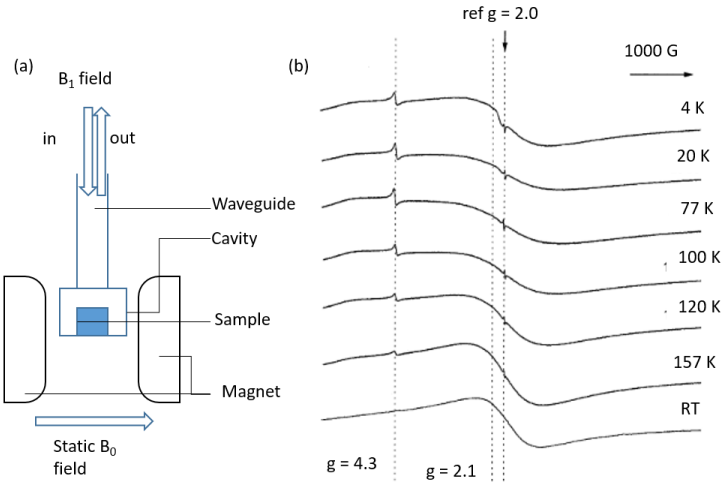

Figure 5: Schematic representation of an EPR setup (a) and signal (b) acquired therewith [21]*. The setup consists of a sample placed in a static B_0 field generated by the field coils. The sample is placed in the cavity and exposed to an oscillating B_1 field guided through the waveguide. Absorbed energy of the standing-wave generated by B_1 in the cavity is measured through the difference of incoming and outgoing B_1 energy. Spectra of HoSF (black lines), measured at different temperatures, are shown in (b) as a function of B_0 (given in Gauss).* ***Permission for reproduction was not asked. Own spectra will replace this later***

Different is Mössbauer spectroscopy, which is based on resonant absorption of gamma rays by Fe nuclei in the samples. This energy absorption occurs in a recoil-free manner, with no lattice vibration (phonons) transmitted to the solid [16]. As depicted in figure 6(a), the unstable nucleus, aligned with the sample, decays to its stable state under emission of gamma-rays of low energy. The gamma-rays in line with the sample interact with the sample in a recoil-free manner – due to the Mössbauer effect.

The dip in figure 6(b) (see ref 51 in [18]) corresponds to the resonant absorption of energy, i.e. minimal transmission. Using the Doppler effect, the photon energy can be tuned over a large range, therefore allowing to detect spectra shifted from the bare conditions (isomer shift) and split by either quadrupole and/or magnetic interaction. For a clear overview on how to interpret Mössbauer spectra in the framework of superparamagnetism, the reader is referred to [17].

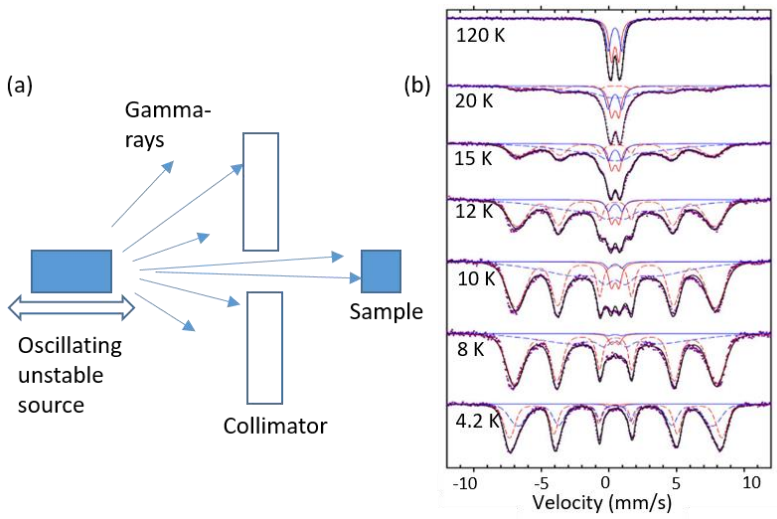

Figure 6: Schematic representation of a Mössbauer spectroscopy setup (a) and signal (b) acquired therewith (ref 51 in [18]*). The setup consists of a rapidly oscillating unstable source, of which decay products are gamma-rays with frequencies that resonate with the resonance frequency of the sample. Gamma-rays with a linear path to the sample allowed to interact with the sample, while those that are not are blocked by a collimator. Absorption spectra are measured at different temperatures (b). Study under different temperatures allows for the study of parameters such as isomer shift, quadrupole splitting and magnetic hyperfine splitting.* ***No permission for reproduction asked.***

3.2.2 Magnetometry

Magnetometry measurements are often used for the analysis of superparamagnetic [16]. Analysis of antiferromagnetic material is also possible at high applied fields B_0. The most sensitive magnetometry techniques use a superconducting quantum interference device (SQUID), where a sample passes through a superconducting ring interrupted in two spots (weak links or Josephson junctions). The Josephson effect makes the device sensitive to the magnetic flux quantum Φ_0= 2.0710−15 Wb, as explained below.

When the ring is biased with a current, a magnetic flux will be induced. However, the flux enclosed by the superconducting loop must be an integer number of flux quanta, therefore, the voltage-flux characteristic of a DC-squid will result in a periodic function of Φ_0, upon application of a current above the critical current of the material.

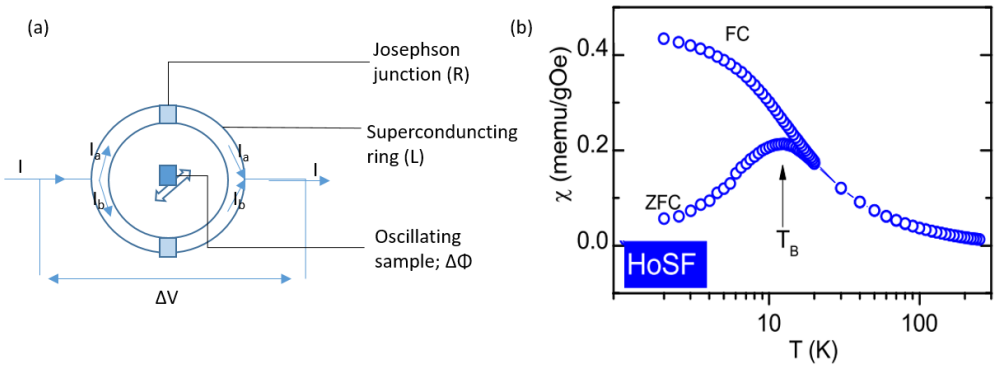

Figure 7: Schematic representation of SQUID detection (a) and signal (b) acquired therewith [22]*. The setup consists of a superconducting ring with self-conductance L and two Josephson junctions – often referred to as 'weak links' – with resistance R. Through each junction a current is led (I_a and I_b, split upon entry and rejoined upon exit of the superconducting ring), and measurement hereof leads to determination of the magnetic flux Φ. Φ is induced by the oscillation of the sample at the centre of the superconducting ring, powered by changes in current through applied altering voltage V. The current, proportional to the net magnetization of the sample, is measured at different temperatures and B_0 field strengths (b). In this manner, ZFC and FC curves can be measured under the relation of magnetic susceptibility as a function of temperature. Here, this was done for HoSF, and average T_B is indicated with an arrow* [22]*.* ***Permission for reproduction was not asked. Own spectra will replace this later.***

Now, by choosing a working point where the derivative of V vs Φ is maximum, the device will be sensitive to tiny changes of magnetic flux, as those induced by a close-by moving magnetic sample.

Schematic setup and signal example (of HoSF [22]) of field strength dependence and temperature of net magnetization are shown in figure 7, as acquired from ZFC/FC measurements.

ZFC/FC measurements - As the name suggests, ZFC refers to the act of cooling the sample from 300 K to a lower temperature in the absence of a magnetic field. This leads to random (i.e. along the anisotropy axis) blocking of magnetic moments of particles of decreasing size. At the target (low) temperature, the magnetic field is applied, and the magnetic moments then measured. Repeating this measurement in the presence of a small magnetic field (generally 50 mT), leads to the acquisition of a FC curve, where the magnetic moments of the particles in the sample are aligned.

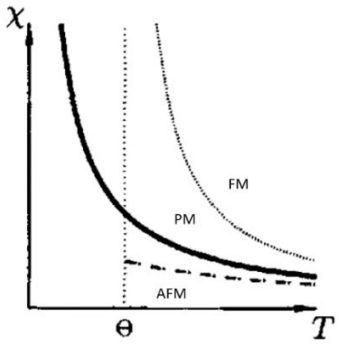

Figure 8: Relation between susceptibility and temperature for ferri- and ferromagnetically ordered (FM; Θ = Curie temperature), paramagnet (PM; Θ = 0) and antiferromagnetically ordered (AFM; Θ = Néel temperature) material, as fitted according to the Curie-Weiss law [16]*. For all, the susceptibility decreases with increasing temperature. The rate at which this occurs is magnetic order dependent.*

Determination type magnetic order - By measuring the susceptibility of a paramagnet at different temperatures, and fitting this data to the Curie-Weiss law the type of magnetic order present in the sample can be determined [23]. As can be seen in figure 8, susceptibility increases more rapidly with decreasing temperature in case of ferri- and ferromagnetic materials than in antiferromagnetic material.

After determination of T_B from ZFC/FC magnetometry measurements, as described in Section 3.3, hysteresis loops can be measured, after an initial ZFC state is reached [24]. Example are shown in figure 9.

Hysteresis loops - Measurements of hysteresis loops indicate the presence of superparamagnetic particles under the influence of temperature. At temperatures above T_B, the hysteresis loop is closed; i.e. purely superparamagnetic behaviour is observed [24]. Below the T_B, the hysteresis loops open and the coercivity – the minimal B strength needed to demagnetize the system – and saturation remanence – magnetization of the system measured are therefore non-null. Opening of hysteresis loops is an indication of antiferromagnetic, ferro- or ferrimagnetic ordering present within the sample. A high coercivity (i.e. a wide hysteresis loop) is characteristic for antiferromagnetic materials, while a low coercivity is characteristic of ferrimagnetic materials. Apart from helping with the identification of possible presence of antiferromagnetic material in the sample, hysteresis loops can also be used, among others, for determination of the exchange bias, present at ferrimagnetic/antiferromagnetic interfaces [25]. The exchange bias effect is observed as a shift of a magnetic hysteresis loop relative to the origin of coordinates, and is attributed to the magnetic interactions at the interface between ferrimagnetic and antiferromagnetic structures. Similar effects are observed in single-phase antiferromagnetic nanoparticles, such as ferritin, where the ferrimagnetic phase can be due to defects and incomplete compensation of the antiferromagnetic sublattices.

Loading factor ferritin and magnetic moment – according to Néel's theory of superparamagnetism, LF of ferritin can be calculated through measurement of the magnetic moment of ferrihydrite (μ_{p_Fh}) using the relation (see ref 48 in [8]):

$$LF = (\mu_{p\_Fh} / 5.92\mu_B)^{(1/\alpha)}, \quad (2)$$

where α ranges between 0.5 and 0.6, and $5.92\mu_B$ is the magnetic moment of Fe^{3+}.

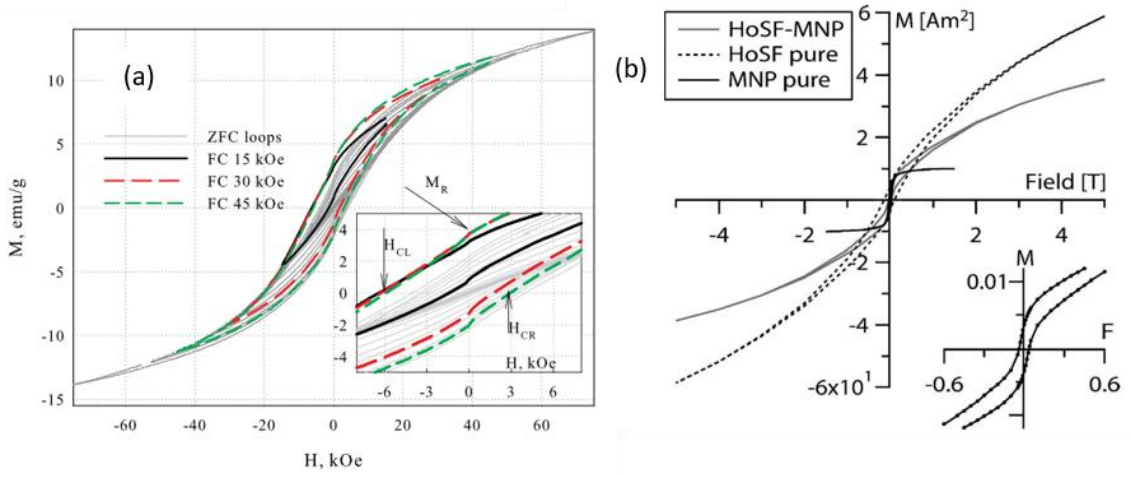

Figure 9: Examples of hysteresis loops acquired for (a) bacterial ferrihydrite [25] *and (b) horse spleen ferritin, magnetite nanoparticle and mixture thereof* [24]. *In (a) the effect of different cooling fields is shown in black, red and green. In the inset left and right coercivity (H_{CL} and H_{CR}) and magnetic remanence (M_R) are indicated. In (b) the effect of magnetic order on measured coercivity is shown. Pure HoSF – which has antiferromagnetic ordering – has a larger coercivity than magnetite nanoparticles (MNP) – which have ferrimagnetic ordering. In the inset, the effect of mixing these two components is shown: a low coercivity combined with a large open hysteresis loop.*

3.2.3 (HR)TEM and EELS

The particle size distribution can be determined using spectroscopy techniques such as (HR)TEM, SEM [6]. Using these techniques the maximum diameter of individual particles in a sample, regardless of inhomogeneities in the sample, can be extracted [6]. These techniques have been extensively used in the study of crystal structures [10].

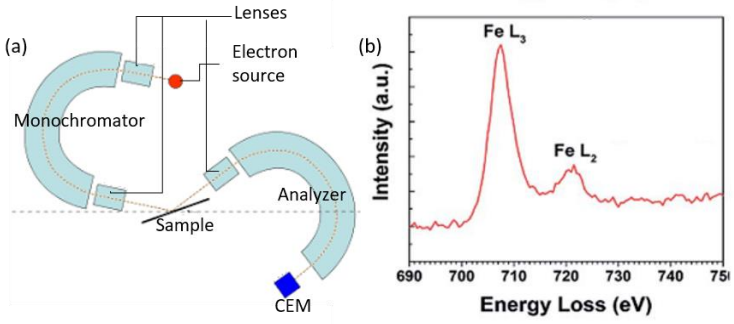

Figure 10: Schematic representation of HR-EELS setup (a) and example of a signal (b), after normalization and background subtraction [28], *are shown. Energy loss of monochromatic energy electrons is measured and analysed after interaction with a sample. Intensities in the signal, dependent on spin orbital occupancy, and energy loss of electron beam emitted electrons are plotted, leading to the characterization of ferritin Fe $L_{3,2}$ edges.* ***Images are both used without permission for reproduction.***

Using (HR)TEM, it is also possible to acquire additional information on individual particles within a sample, by combining it with EELS [26]. Upon combination of these two techniques, particle sizes and crystal structure (by HRTEM) can be matched with elemental and chemical compositions and oxidation states (by EELS). This matching takes place on individual particle level. Using this method at high resolutions, spatial element identification and relative proportion valence states in mixed valence

samples can be determined on single atomic level [26]. In the case of ferritin, one is interested in the ratio of Fe^{3+} and Fe^{2+} present inside the cavity, and from this ratio determine which minerals are present or, on an individual level, determine which mineral is observed and its abundance inside the sample [27].

A schematic representation of HR-EELS is shown in figure 10(a). As can be seen, monochromatic energy electrons emitted by an electron source are measured and analysed after interaction with a sample. An example of a spectrum is given in figure 10(b), where the energy loss of electrons is plotted against the edge signal intensity. This intensity is dependent on spin orbital occupancy. Through comparison of spectra belonging to samples of known chemical composition, presence or absence of specific phases of Fe can be determined [28].

Table 2: Table indicating temperature usage, field usage, measurement frequency range and measurement parameters for different techniques used for measurement of magnetic properties of ferritin.

Method	Measures	Measurement frequency (ν) range	B field usage [T]
Nuclear magnetic resonance (NMR) and MRI *	Isomer shift δ, relaxation times, spin-spin coupling, magnetization M, indirectly: relative susceptibility χ	9.7 – 32.3 MHz [29]	7 – 23 T [29]
Electron paramagnetic resonance (EPR) *	g-tensor, hyperfine interaction of paramagnetic centres: structure, ligand environment, magnetization M, relaxation times	1.1 (L-band) – 94 (W-band) GHz [30] Conventional: 9.5 GHz (X-band)	0T – 3.3T (maximum depends on device) Conventional: 0T – 0.3 T (X-band) [22]
Mössbauer spectroscopy	Isomer shift δ, quadrupole splitting, magnetic hyperfine splitting	10^8 Hz range	-
SQUID Magnetometry	$M(B_0,T)$, $M(B,T_0)$ -> maximum T_B + minimum particle sizes distribution upon further T lowering, $\chi(B_0, T)$, hysteresis curve	DC: ν < 100 Hz AC: 100 Hz < ν < 1kHz	Generally: 0 – 7 T

* For both NMR and EPR, it is possible to acquire the spectra using continuous wave (CW) and pulsed wave (PW) mode. In CW resonance, the frequency of an oscillation magnetic field with linearly increasing strength is kept constant. In PW the strength of the oscillating magnetic field is kept constant while the frequency of the oscillation is linearly increased.

3.3 Determination of blocking temperature using different measurement techniques

When the characteristic time of a measurement technique τ_M equals τ_N, the magnetic moment undergoes an apparent blocking. The 'blocking temperature' (T_B) can be obtained after rewriting of equation 1 as

$$T_B = KV/(k_B \ln(\tau_M/\tau_0)) . \quad (3)$$

At and below this temperature, flipping of the magnetic moments of the nanoparticle, such as the ferritin core, is no longer perceived, and the particle is referred to as "blocked".

It has been shown, in studies focusing on commercially available horse spleen ferritin (HoSF), that it is possible to determine τ_0 and the intrinsic ferritin property K simultaneously (see refs 32 and 87 in [18]). This was done by combining the results from magnetometry and Mössbauer observations. By combining DC magnetometry (static) with AC susceptibility (dynamic), Mössbauer spectroscopy and TEM it is possible to determine the mean particle volume in the sample, K and τ_0 with high accuracy (see ref 41 in [18]). Similarly, K has also been determined for bulk nanocrystals maghemite (see ref 65 in [22]) and magnetite (see ref 66 in [22]), and can be used as an approximate K in the analysis of human ferritin. Using magnetometry measurements, the peak of the zero-field-cooled (ZFC) χ-curve versus temperature indicates the T_B of the average particle size present in the sample, whereas the bifurcation of the ZFC and field-cooled (FC) curves indicate the temperature above which all particles in the sample – including those with the largest size – behave superparamagnetically [24].

T_B can also be measured with Mössbauer spectroscopy and EPR.

When the intrinsic particle properties K, V and τ_0 are known for a sample, the relation between T_B and τ_M, or alternative T_B and characteristic measurement frequency unique to the technique at hand, can be described by equation 3, as indicated in figure 11. Here KV/k_B was assumed equal to 339 K, as proposed in Ref 33 in [18] for horse spleen ferritin, and τ_0 ranged between 10^{-11} s (red in figure 11) and 10^{-13} s (black in figure 11). Measured blocking temperatures are expected to range between these boundaries.

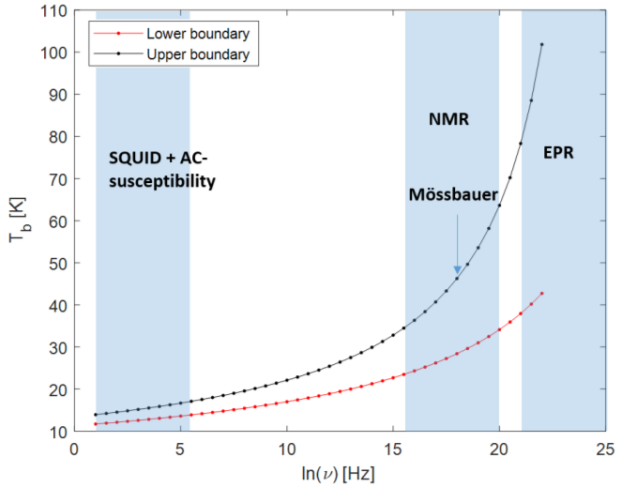

Figure 11: Theoretical relation between T_B and ln(frequency), described by equation 3 and acquired under assumed KV/k_B = 339 K [from ref 33 in [18]*]. Lower (red; $\tau_0 = 10^{-11}$ s) and upper (black; $\tau_0 = 10^{-13}$ s) T_B limits, between which measured T_B values are expected, are plotted. In blue the ln(frequency) ranges belonging to SQUID magnetometry and AC-susceptibility, NMR, Mössbauer spectrometry (arrow) and EPR are indicated.*

The range of measured T_B expected per technique used is indicated in blue for SQUID and AC-susceptibility, NMR and EPR measurements, and is indicated with an arrow for Mössbauer spectroscopy.

3.4 From blocking temperature to critical diameter

T_B indicates the minimum size of particles that are no longer perceived as behaving superparamagnetically at a certain temperature. By looking at equation 3 for a fixed system and sample – τ_M and K are constant – with a particle size distribution, blocked particle volume can be defined as a function of temperature. Under assumption of the particle shape of volume V, then, the critical diameter of blocked particles can be described.

Through magnetization measurements, such as determination of susceptibility, particle size distribution can be. Knowledge of these distributions can further be used in the determination of iron particle concentrations in mixed samples [22].

4. Present day knowledge on Ferritin

In order to be able to detect the presence of ferritin and identify the minerals inside its core, the magnetic properties of the ferritin core and the effect of the minerals therein need to be understood. In the following sections, the effect of iron loading on relaxation times and the results of determination of particle distribution and elemental composition are discussed. Also susceptibility measurements and electron spin measurements are discussed. Finally, specific aspects related to brain iron as measured with MRI are mentioned.

4.1 Iron loading dependence of relaxation times

In figure 4(b) the measured effect of LF on r_1 is shown. LF is found to naturally increase both as the brain ages [2], and in the presence and progression of certain forms of neurodegeneration (e.g. [8]).

Based on their findings of r_2 dependence on LF of apoferritin, Nandwana et al. suggested that relaxivity data might aid the understanding of the process behind the formation of the magnetic core in ferritin [28]. According to their proposed model there is almost no contribution to the development of the magnetic core when LF is less than 2400, as most of the iron atoms would initially gather near the inner shell surface. The r_2 increase after further loading of the core was ascribed to the development of the superparamagnetic core. After full loading the r_2 signal had doubled compared to the signal at lower LF rates. Strangely, the r_1 did not increase much throughout the loading.

Due to its surface properties, structure and biocompatibilities [31], [32], ferritin has been extensively studied for its possible usage as a contrast agent in MRI. Although the LF, and thus r_2 signal, is generally too low to induce a contrast above the noise level. It has been suggested that the r_2 signal could be improved through ferritin aggregation and polymerized ligand binding to actin [33]. Generally, however, focus of these studies is placed on magnetoferritin, the superparamagnetic nanoparticle synthesized through loading of apoferritin with magnetite and/or maghemite [32]. Magnetoferritin has much higher relaxivities than natural ferritin, due to the strength of the core magnetization (see refs 36 and 37 in [28]). For an overview on the synthesis, magnetic properties and biomedical applications of magnetoferritin, the review by Xue et al. is recommended [9].

4.2 Particle size distribution and elemental composition

Dysfunction of ferritin shell H subunits could be cause of alterations in mineral concentrations in the core, as Fe^{2+} is not properly converted to Fe^{3+} [1]. This would, by combining EELS with HRTEM, be observed with a decrease in hexagonal phase structures characteristic of ferrihydrite and hematite, and an increase in cubic shape characteristic of magnetite and maghemite. Indeed, this has observed under comparison of physiological and pathological ferritin cores [1], [34], [35]. It has been suggested, however, that these techniques might lead to a misinterpretation of the mineral concentrations present inside the sample, due to the high energies of the electron beams used with EELS [36]. These energies might be high enough to partially convert the octahedral coordination around iron to a tetrahedral coordination, leading to an observed cubic shape where initially was a hexagonal shape. However, it is unlikely that this structural change induced by the electron beam would preferential affect pathological ferritins.

4.3 Susceptibility measurements indicate magnetic order

It has been shown that for susceptibility measurements of ferritin at varying temperature, χ decreases with increasing temperature under the influence of external magnetic fields up to 6 T, as expected for an antiferromagnetic system [37]. On inspection of ferrihydrite in magnetic fields increasing up to 25 T, χ similarly initially decreases with increasing temperature for magnetic fields below 6 T [38]**.** However, with further increase of the magnetic field χ decreases less per increment temperature. This behaviour is typical for systems of antiferromagnetic particles with random orientation of the crystallographic axes, and occurs due to the presence of small uncompensated magnetic moments within both the surface and bulk of the mineral [39]. This superparamagnetic behaviour is described as a superposition of Langevin functions. The magnetic anisotropy K of ferrihydrite consists of both a bulk and surface anisotropy. It has been suggested that ferrihydrite might have an antiferromagnetic core with a superparamagnetic surface [10].

Most *in vitro* magnetization studies of ferritin are performed using magnetometry measurements- specifically using SQUID - and EPR.

In figure 9 hysteresis curves acquired on (a) bacterial ferrihydrite [25] and on (b) HoSF, magnetite nanoparticles and a mixture thereof [24] are shown. In figure 9(a) the effect of different cooling fields is shown in black, red and green, and in the insert the coercivity and magnetic remanence of the material are indicated. In figure 9(b) the effect of magnetic order on coercivity is shown. Figure 9(b) lead to the conclusion that a mixture of HoSF and magnetite nanoparticles mimic the magnetic properties of human brain tissue well [24].

4.4 Probing the iron electron spins of ferritin nanoparticles

Although most EPR studies on ferritin focus on describing changes of the shape of the spectrum rather on the interpretation of the origin of the features, there is a consensus on what the shape of a ferritin EPR spectrum looks like (e.g. [21], [40], [41], [42]).

Figure 5(b) shows that the spectra of ferritin are broad and that the lineshape changes as a function of the temperature. There is a narrow peak with relatively small intensity at g = 4.3, and a broader signal with higher intensity around g = 2.0. Figure 12(a) shows the signal around g = 2.0, observed from iron-loaded human spleen ferritin [40] rather than HoSF [21], where the broad signal is composed of two

overlapping broad signals, indicated with A (low-field feature) and B (high-field feature) [21], [40]. Feature B is centred around g = 2.0.

The interpretation of the features observed is still under debate [40], [42]. Here, the interpretation proposed by Weir et al. is described. Weir et al. proposed that the signal at g = 4.3 is due to rhombohedric high spin Fe^{3+}, while the broad signals A and B are due to the ferrihydrite core [40]. They suggested, though simulations, that feature A could be described as a hexagonal ferromagnetic-type resonance from cores below their blocking temperatures [40]. Their simulation of feature A, in comparison to a measured spectrum, is shown in figure 12(b)**.** Again, feature A and B are indicated with arrows.

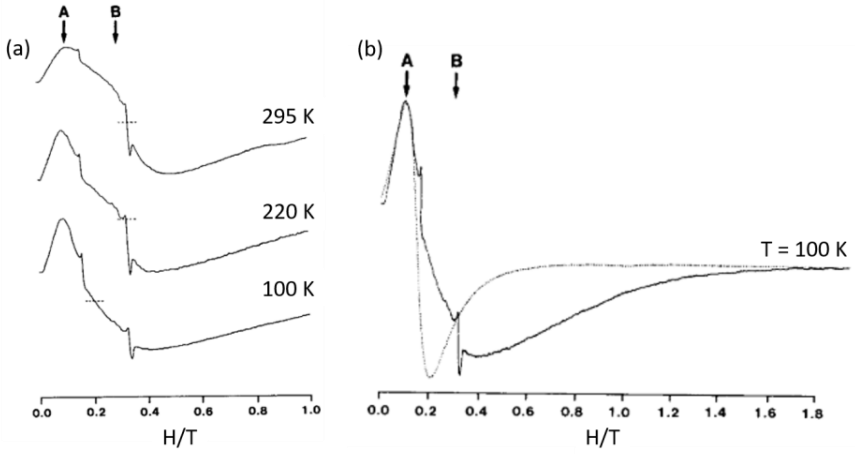

Figure 12: EPR spectra of ferritin isolated from iron-loaded human spleens, as a function of the temperature normalized magnetic field H [40]*. The low-field and high-field broad features caused by the ferrihydrite core are indicated with arrows A and B respectively. In figure (a) the lineshape change of these features can be seen under influence of changes in temperature. In figure (b) feature A is simulated as a hexagonal ferromagnetic-type resonance from cores below their blocking temperatures (dashed line) on top of the original signal acquired at temperature T = 100 K (solid line).*

Weir et al. assigned feature A to the signal of blocked ferritin cores and feature B to the signal of unblocked ferritin cores [40]. Since more cores become blocked upon lowering of the temperature, this explains the observed increase in intensity of feature A upon decrease of the temperature and the decrease of feature B. This change in intensity has also been observed by other studies [21], [41]. Weir et al. also discuss the increase in intensity of feature A and decrease of feature B upon increase of the LF of the ferritin cores [40]. A relation between the broad features and superparamagnetic behaviour of the ferritin cores has therefore been suggested [41].

The above findings are in line with what we would expect of superparamagnetic ferrihydrite nanoparticles, as the magnetic moment of ferrihydrite increases with LF due to an increase of the mineral size. Due to the linear relation between core size and T_B, it can be seen that T_B will increase as the LF increases. Similarly, equation 3 shows that by measuring a system at decreasing temperatures cores of decreasing volumes will be blocked. An increase in signal intensity of blocked cores would therefore be expected upon temperature decrease or LF increase, as more unpaired electrons in the system would get blocked along the direction of the magnetic field.

4.5 Specific aspects related to brain iron

MRI can be used to study the magnetic susceptibility of a sample, via the interaction between the nuclei under investigation and the electron system of interest. Given the experimental setup that MRI offers, measurements on ferritin can be performed both *in vivo* and *in vitro,* (clinic (e.g. [43])) and post-mortem (e.g. [28]). Susceptibility measurements, used for distinction between paramagnetic and diamagnetic material in the subject at room temperature, can be performed indirectly with tools such as susceptibility weighted imaging (SWI) [44] and quantitative susceptibility mapping (QSM) [44]. These protocols allow for acquisition of high resolution images that are informative on iron spatial localisation, making it possible to detect brain iron abnormalities [45].

Although MRI studies performed exclusively at body temperature might somewhat limit the study of ferritin's magnetic properties, it is generally sufficient in a clinical setting. In [46] is described that several factors, such as the presence of myelin and possible additional pathological effects which introduce other trace metals, have to be considered as possible sources of paramagnetic signal, as they limit the accuracy of these MRI techniques in certain tissues. Improvement of QSM accuracy and possibility of true phase imaging was attempted, and seems promising [47].

5. Conclusion

Ferritin is interesting for both medical and nanoscience applications. For this reason, it has been extensively studied throughout the past 70 years, and this literature study is a summary of the published work aimed at unravelling ferritin complex magnetic properties.

Although the minerals inside the ferritin core each have their own magnetic order, they each behave superparamagnetically above their individual blocking temperature, due to uncompensated spins present on their surfaces. These T_B are dependent on particle properties, such as particle size, magnetic anisotropy and characteristic relaxation time, and on the characteristic time of the measurement technique used.

In order to probe the magnetic properties of ferritin, measurements should be performed both above and below T_B unique to the minerals present therein. These measurements can focus both on the magnetic moments of nuclei or electrons, and on oxidation states present in the sample.

Nuclear spin relaxation times have been found to show dependence on the amount of iron loaded into the ferritin protein. This dependence can potentially be of use in the development of biocompatible contrast agents in MRI and as a pathological biomarker in the detection and development of neurodegenerative diseases.

Particle size distribution and elemental and chemical composition can be determined mainly via electron microscopy and EELS. These techniques allow for the determination of elemental ratios, such as the concentrations of Fe^{3+} and Fe^{2+} present in a sample. Comparison of EELS spectra with those obtained from samples of known chemical and crystal composition may allow the speciation of iron and its abundance in the core of ferritin.
Through determination of magnetic susceptibility in experimental setups generally with SQUID magnetometry, one can determine and distinguish, among others, different magnetic orders present in the sample.

Direct investigation of the iron magnetic moment in the ferritin sample can be carried out with Mössbauer spectroscopy and EPR. The latter provides direct information on the crystal and ligand structure of the iron spins.

As each of these techniques has different sensitivities, we foresee that new insights on the magnetic properties of ferritin can be gained through complementation of multiple techniques.

Bibliography

[1] C. Quintana and L. Gutiérrez, "Could a dysfunction of ferritin be a determinant factor in the aetiology of some neurodegenerative diseases?," *Biochimica et Biophysica Acta - General Subjects*, vol. 1800, no. 8. pp. 770–782, Aug-2010, doi: 10.1016/j.bbagen.2010.04.012.

[2] J. Acosta-Cabronero, M. J. Betts, A. Cardenas-Blanco, S. Yang, and P. J. Nestor, "In vivo MRI mapping of brain iron deposition across the adult lifespan," *J. Neurosci.*, vol. 36, no. 2, pp. 364–374, Jan. 2016, doi: 10.1523/JNEUROSCI.1907-15.2016.

[3] S. A. You and Q. Wang, "Ferritin in atherosclerosis," *Clinica Chimica Acta*, vol. 357, no. 1. pp. 1–16, 01-Jul-2005, doi: 10.1016/j.cccn.2005.02.001.

[4] J. R. Connor, B. S. Snyder, P. Arosio, D. A. Loeffler, and P. LeWitt, "A Quantitative Analysis of Isoferritins in Select Regions of Aged, Parkinsonian, and Alzheimer's Diseased Brains," *J. Neurochem.*, 1995, doi: 10.1046/j.1471-4159.1995.65020717.x.

[5] M. Mehlenbacher *et al.*, "Iron Oxidation and Core Formation in Recombinant Heteropolymeric Human Ferritins," *Biochemistry*, vol. 56, no. 30, pp. 3900–3912, Aug. 2017, doi: 10.1021/acs.biochem.7b00024.

[6] S. Narayanan, R. Shahbazian-Yassar, and T. Shokuhfar, "Transmission electron microscopy of the iron oxide core in ferritin proteins: Current status and future directions," *Journal of Physics D: Applied Physics*, vol. 52, no. 45. Institute of Physics Publishing, 22-Aug-2019, doi: 10.1088/1361-6463/ab353b.

[7] F. Bou-Abdallah *et al.*, "Ferritin exhibits Michaelis-Menten behavior with oxygen but not with iron during iron oxidation and core mineralization," *Metallomics*, 2019, doi: 10.1039/c9mt00001a.

[8] M. Bulk *et al.*, "Quantitative comparison of different iron forms in the temporal cortex of Alzheimer patients and control subjects," *Sci. Rep.*, vol. 8, no. 1, Dec. 2018, doi: 10.1038/s41598-018-25021-7.

[9] L. Xue, D. Deng, and J. Sun, "Magnetoferritin: Process, Prospects, and Their Biomedical Applications," *International journal of molecular sciences*, vol. 20, no. 10. NLM (Medline), 16-May-2019, doi: 10.3390/ijms20102426.

[10] T. Hiemstra, "Surface structure controlling nanoparticle behavior: Magnetism of ferrihydrite, magnetite, and maghemite," *Environ. Sci. Nano*, vol. 5, no. 3, pp. 752–764, 2018, doi: 10.1039/c7en01060e.

[11] A. García-Prieto *et al.*, "On the mineral core of ferritin-like proteins: Structural and magnetic characterization," *Nanoscale*, 2016, doi: 10.1039/c5nr04446d.

[12] Y. Gossuin, P. Gillis, A. Hocq, Q. L. Vuong, and A. Roch, "Magnetic resonance relaxation properties of superparamagnetic particles.," *Wiley Interdiscip. Rev. Nanomed. Nanobiotechnol.*, vol. 1, no. 3, pp. 299–310, May 2009, doi: 10.1002/wnan.36.

[13] R. A. Brooks, J. Vymazal, R. B. Goldfarb, J. W. M. Bulte, and P. Aisen, "Relaxometry and magnetometry of ferritin," *Magn. Reson. Med.*, vol. 40, no. 2, pp. 227–235, Aug. 1998, doi: 10.1002/mrm.1910400208.

[14] M. Gusenbauer and N. R. Haddaway, "Which Academic Search Systems are Suitable for Systematic Reviews or Meta-Analyses? Evaluating Retrieval Qualities of Google Scholar, PubMed and 26 other Resources," *Res. Synth. Methods*, p. jrsm.1378, Oct. 2019, doi: 10.1002/jrsm.1378.

[15] N. J. Van Eck and L. Waltman, "VOSviewer," *Leiden.: CWTS*, 2020. [Online]. Available: https://www.vosviewer.com/. [Accessed: 16-Feb-2020].

[16] S. Blundell, "Magnetism in Condensed Matter," *OXFORD Univ. Press*, vol. 1, pp. 1–228, 2001, doi: 10.1017/CBO9781107415324.004.

[17] C. Hawkins, J. M. Williams, A. J. Hudson, S. C. Andrews, and A. Treffry, "Mössbauer studies of the ultrafine antiferromagnetic cores of ferritin," *Hyperfine Interact.*, vol. 91, no. 1, pp. 827–833, Dec. 1994, doi: 10.1007/BF02064614.

[18] G. C. Papaefthymiou, "The Mössbauer and magnetic properties of ferritin cores," *Biochimica et Biophysica Acta - General Subjects*, vol. 1800, no. 8. pp. 886–897, Aug-2010, doi: 10.1016/j.bbagen.2010.03.018.

[19] L. Bossoni *et al.*, "Human-brain ferritin studied by muon spin rotation: A pilot study," *J. Phys. Condens. Matter*, vol. 29, no. 41, Sep. 2017, doi: 10.1088/1361-648X/aa80b3.

[20] M. Brustolon and E. Giamello, *Electron Paramagnetic Resonance: A Practitioner's Toolkit*. Hoboken, NJ, USA: John Wiley and Sons, 2008.

[21] S. Aime *et al.*, "EPR investigations of the iron domain in neuromelanin," *Biochim. Biophys. Acta - Mol. Basis Dis.*, vol. 1361, no. 1, pp. 49–58, Jul. 1997, doi: 10.1016/S0925-4439(97)00014-8.

[22] P. Kumar *et al.*, "A novel approach to quantify different iron forms in ex-vivo human brain tissue," *Sci. Rep.*, vol. 6, Dec. 2016, doi: 10.1038/srep38916.

[23] C. Birkl *et al.*, "Iron mapping using the temperature dependency of the magnetic susceptibility," *Magn. Reson. Med.*, vol. 73, no. 3, pp. 1282–1288, Mar. 2015, doi: 10.1002/mrm.25236.

[24] F. Brem, L. Tiefenauer, A. Fink, J. Dobson, and A. M. Hirt, "A mixture of ferritin and magnetite nanoparticles mimics the magnetic properties of human brain tissue," *Phys. Rev. B - Condens. Matter Mater. Phys.*, vol. 73, no. 22, 2006, doi: 10.1103/PhysRevB.73.224427.

[25] D. A. Balaev *et al.*, "Exchange bias in nano-ferrihydrite," *J. Appl. Phys.*, vol. 120, no. 18, Nov. 2016, doi: 10.1063/1.4967912.

[26] C. C. Calvert, A. Brown, and R. Brydson, "Determination of the local chemistry of iron in inorganic and organic materials," *J. Electron Spectros. Relat. Phenomena*, vol. 143, no. 2-3 SPEC. ISS., pp. 173–187, May 2005, doi: 10.1016/j.elspec.2004.03.012.

[27] N. Gálvez *et al.*, "Comparative structural and chemical studies of ferritin cores with gradual removal of their iron contents," *J. Am. Chem. Soc.*, 2008, doi: 10.1021/ja800492z.

[28] V. Nandwana *et al.*, "Engineered ferritin nanocages as natural contrast agents in magnetic resonance imaging," *RSC Adv.*, vol. 7, no. 55, pp. 34892–34900, 2017, doi: 10.1039/c7ra05681h.

[29] Bruker Corporation, "NMR Frequency Tables," 2012. [Online]. Available: http://kodu.ut.ee/~laurit/AK2/NMR_tables_Bruker2012.pdf.

[30] F. Moro *et al.*, "Magnetic anisotropy of polycrystalline magnetoferritin investigated by SQUID and

electron magnetic resonance," *J. Magn. Magn. Mater.*, vol. 361, pp. 188–196, 2014, doi: 10.1016/j.jmmm.2014.02.053.

[31] J. W. M. Bulte *et al.*, "Magnetoferritin: Characterization of a novel superparamagnetic MR contrast agent," *J. Magn. Reson. Imaging*, vol. 4, no. 3, pp. 497–505, 1994, doi: 10.1002/jmri.1880040343.

[32] M. R. Ruggiero, D. Alberti, V. Bitonto, and S. G. Crich, "Ferritin: A platform for MRI contrast agents delivery," *Inorganics*, vol. 7, no. 3. MDPI Multidisciplinary Digital Publishing Institute, 2019, doi: 10.3390/INORGANICS7030033.

[33] K. M. Bennett, E. M. Shapiro, C. H. Sotak, and A. P. Koretsky, "Controlled aggregation of ferritin to modulate MRI relaxivity," *Biophys. J.*, vol. 95, no. 1, pp. 342–351, Jul. 2008, doi: 10.1529/biophysj.107.116145.

[34] C. Quintana *et al.*, "Initial studies with high resolution TEM and electron energy loss spectroscopy studies of ferritin cores extracted from brains of patients with progressive supranuclear palsy and Alzheimer disease.," *Cell. Mol. Biol. (Noisy-le-grand).*, vol. 46, no. 4, pp. 807–820, 2000.

[35] C. Quintana, J. M. Cowley, and C. Marhic, "Electron nanodiffraction and high-resolution electron microscopy studies of the structure and composition of physiological and pathological ferritin," *J. Struct. Biol.*, vol. 147, no. 2, pp. 166–178, Aug. 2004, doi: 10.1016/j.jsb.2004.03.001.

[36] Y. H. Pan *et al.*, "3D morphology of the human hepatic ferritin mineral core: New evidence for a subunit structure revealed by single particle analysis of HAADF-STEM images," *J. Struct. Biol.*, vol. 166, no. 1, pp. 22–31, Apr. 2009, doi: 10.1016/j.jsb.2008.12.001.

[37] N. J. O. Silva, V. S. Amaral, and L. D. Carlos, "Relevance of magnetic moment distribution and scaling law methods to study the magnetic behavior of antiferromagnetic nanoparticles: Application to ferritin," *Phys. Rev. B - Condens. Matter Mater. Phys.*, vol. 71, no. 18, 2005, doi: 10.1103/PhysRevB.71.184408.

[38] D. A. Balaev *et al.*, "Temperature Behavior of the Antiferromagnetic Susceptibility of Nanoferrihydrite from the Measurements of the Magnetization Curves in Fields of up to 250 kOe," *Phys. Solid State*, vol. 59, no. 8, pp. 1547–1552, Aug. 2017, doi: 10.1134/S1063783417100031.

[39] D. A. Balaev *et al.*, "Magnetic properties of heat treated bacterial ferrihydrite nanoparticles," *J. Magn. Magn. Mater.*, vol. 410, pp. 171–180, Jul. 2016, doi: 10.1016/j.jmmm.2016.02.059.

[40] M. P. Weir, T. J. Peters, and J. F. Gibson, "Electron spin resonance studies of splenic ferritin and haemosiderin," *Biochim. Biophys. Acta (BBA)/Protein Struct. Mol.*, vol. 828, no. 3, pp. 298–305, Apr. 1985, doi: 10.1016/0167-4838(85)90311-5.

[41] E. Wajnberg, L. J. El-Jaick, M. P. Linhares, and D. M. S. Esquivel, "Ferromagnetic resonance of horse spleen ferritin: Core blocking and surface ordering temperatures," *J. Magn. Reson.*, 2001, doi: 10.1006/jmre.2001.2430.

[42] I.V. Alenkina *et al.*, "57Fe Mössbauer spectroscopy and electron paramagnetic resonance studies of human liver ferritin, Ferrum Lek and Maltofer®," Spectrochimica Acta - Part A: Molecular and Biomolecular Spectroscopy, vol. 130, pp. 24-36, Sept. 2014, doi: 10.1016/j.saa.2014.03.049.

[43] Q. Chen *et al.*, "Iron deposition in Parkinson's disease by quantitative susceptibility mapping,"

BMC Neurosci., 2019, doi: 10.1186/s12868-019-0505-9.

[44] E. M. Haacke *et al.*, "Establishing a baseline phase behavior in magnetic resonance imaging to determine normal vs. abnormal iron content in the brain," *J. Magn. Reson. Imaging*, vol. 26, no. 2, pp. 256–264, Aug. 2007, doi: 10.1002/jmri.22987.

[45] L. De Rochefort, R. Brown, M. R. Prince, and Y. Wang, "Quantitative MR susceptibility mapping using piece-wise constant regularized inversion of the magnetic field," *Magn. Reson. Med.*, 2008, doi: 10.1002/mrm.21710.

[46] S. Ropele and C. Langkammer, "Iron quantification with susceptibility," *NMR in Biomedicine*, vol. 30, no. 4. John Wiley and Sons Ltd, 01-Apr-2017, doi: 10.1002/nbm.3534.

[47] H. Jang *et al.*, "True phase quantitative susceptibility mapping using continuous single-point imaging: a feasibility study," *Magn. Reson. Med.*, vol. 81, no. 3, pp. 1907–1914, Mar. 2019, doi: 10.1002/mrm.27515.